



Bifunctional catalysts based on carbon-coated manganese microspheres applied in the heterogeneous electro-fenton process for tetracycline degradation

Edgar Fajardo-Puerto^a, Abdelhakim Elmouwahidi^{a,*} , Juan Amaro-Gahete^{a,*} ,
 María Pérez-Cadenas^{a,b} , Esther Bailón-García^a , Agustín F. Pérez-Cadenas^a ,
 Francisco Carrasco-Marín^a 

^a *Materiales Polifuncionales Basados en Carbono (UGR-Carbon), Departamento de Química Inorgánica-Unidad de Excelencia Química Aplicada a Biomedicina y Medioambiente-Universidad de Granada (UEQ-UGR), Granada ES18071, Spain*

^b *Departamento de Química Inorgánica y Técnica, Facultad de Ciencias, UNED, Avenida De Esparta s/n, Las Rozas de Madrid, Madrid ES28232, Spain*

ARTICLE INFO

Keywords:

Carbon-coated manganese microspheres
 Oxygen reduction reaction
 Bifunctional electro-Fenton catalyst
 TC degradation

ABSTRACT

Antibiotic contamination in water is a major threat to public health and ecosystems, driven by the spread of resistant bacteria and challenges in treating diseases. Tetracycline (TC), a widely used and persistent antibiotic, has prompted the development of advanced oxidation processes like electro-Fenton for its removal. In this study, carbon-coated manganese microspheres were synthesized as bifunctional electro-Fenton catalysts capable of carrying out oxygen reduction reaction (ORR) and TC degradation in the same electrochemical process. The C90Mn10 formulation, with a high carbon xerogel content, exhibited excellent ORR activity and achieved 90 % TC degradation after 300 min of treatment. This performance was attributed to the synergistic activity of $\text{Mn}^{2+}/\text{Mn}^{3+}$ species and the carbon xerogel in generating hydroxyl radicals via direct and indirect pathways. The catalyst demonstrated stable performance over multiple cycles, maintaining structural integrity and resisting leaching due to the carbon coating. These findings underscore the potential of carbon-coated manganese catalysts as efficient and scalable solutions for removing pharmaceutical contaminants like TC from wastewater.

1. Introduction

The contamination of aquatic environments by pharmaceutical residues has become a critical global issue in recent decades [1]. Among these pollutants, antibiotics represent a particularly worrisome class due to their widespread use and persistence in the environment [2,3]. These substances, designed to inhibit or kill microorganisms, often remain intact after passing through conventional wastewater treatment plants, leading to their accumulation in natural water systems [4]. The presence of antibiotics in water sources poses significant risks, not only by promoting the development of antibiotic-resistant bacteria but also by disrupting microbial ecosystems essential for water quality and environmental balance [5,6].

Tetracycline (TC), a broad-spectrum antibiotic widely employed in both human and veterinary medicine, is one of the most frequently detected pharmaceutical contaminants in wastewater from various

sources, including hospitals, agricultural runoff, and municipal sewage systems, due to its high production volume and limited biodegradability [7,8]. Concentrations of TC in water bodies have been found to vary significantly, often reaching levels that pose risks to both ecosystems and human health [9,10]. Wastewater treatment plants, particularly those processing hospital and industrial effluents, frequently discharge water containing residual amounts of TC, as conventional treatment methods are not fully effective in its removal [11]. Given its persistence and potential ecotoxicological impacts, the development of more advanced water treatment technologies is crucial for fully degrading such compounds, as conventional methods have shown limited effectiveness [12]. Addressing TC contamination in wastewater is therefore a key priority in minimizing the associated environmental and health risks. Thus, there is an urgent need for advanced and efficient technologies capable of degrading these persistent pollutants.

Among the most promising solutions are advanced oxidation

* Corresponding authors.

E-mail addresses: aelmouwahidi@ugr.es (A. Elmouwahidi), j.amarogahete@ugr.es (J. Amaro-Gahete).

<https://doi.org/10.1016/j.jece.2025.115725>

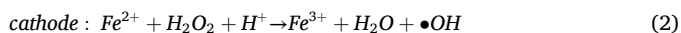
Received 21 November 2024; Received in revised form 13 January 2025; Accepted 4 February 2025

Available online 5 February 2025

2213-3437/© 2025 Elsevier Ltd. All rights are reserved, including those for text and data mining, AI training, and similar technologies.

processes (AOPs), which have demonstrated significant potential in the degradation of a wide range of organic contaminants, including pharmaceuticals like TC [13–16]. AOPs rely on the generation of highly reactive species, such as hydroxyl radicals ($\bullet\text{OH}$), which possess the ability to break down complex organic molecules into simpler, non-toxic compounds. These processes encompass a variety of methods, such as ozonation [17], photocatalysis [18], Fenton reactions [19], and persulfate activation [20], each with its own strengths and limitations depending on the application. While methods like ozonation and photocatalysis are effective, they often come with challenges such as high energy costs or limited scalability in large-scale wastewater treatment. On the other hand, Fenton-based reactions have gained particular attention due to their operational simplicity and high efficiency in generating $\bullet\text{OH}$. However, traditional Fenton processes presents three notable limitations: a restricted operational pH range, elevated costs and risks tied to the management, transport, and storage of reagents (H_2O_2 and iron solutions), and the issue of secondary pollution caused by substantial iron sludge production [21].

To address these drawbacks, the heterogeneous electro-Fenton (HEF) reaction has emerged as an enhanced technique, offering more sustainable and controllable wastewater treatment by generating hydrogen peroxide (H_2O_2) in situ through the oxygen reduction reaction (ORR) at the cathode [22]. This innovation not only eliminates the need for external H_2O_2 addition but also promotes the concurrent reduction of ferric ions (Fe^{3+}) to ferrous ions (Fe^{2+}) at the same electrode diminishing the production of sludge, thereby enhancing the availability of reactive species and overall process efficiency. The electro-Fenton mechanism unfolds through several key stages [23,24]: i) electro generation of H_2O_2 (Eq. 1): At the cathode, dissolved oxygen (O_2) undergoes reduction, leading to the formation of hydrogen peroxide (H_2O_2); ii) generation of the oxidizing $\bullet\text{OH}$ (Eq. 2): In the Fenton reaction, ferrous ions (Fe^{2+}) react with the electrogenerated H_2O_2 in the presence of protons (H^+), producing $\bullet\text{OH}$, highly reactive species responsible for the oxidative degradation of the pollutants; iii) mineralization of pollutants (Eq. 3): $\bullet\text{OH}$ species degrade the pollutant generating less toxic intermediates, carbon dioxide and water; and iv) regeneration of Fe^{2+} : The reduction of ferric ions (Fe^{3+}) back to ferrous ions (Fe^{2+}) at the cathode ensures a continuous supply of Fe^{2+} for the Fenton reaction (Eq. 4).



In this context, it is essential to account for the potential side reactions from water electrolysis as these can negatively impact catalytic performance; however, even greater emphasis should be placed on the choice of cathode materials given that the ORR often represents the rate-limiting step which significantly influences both the efficiency and selectivity of the overall process. The ORR can proceed via different electron pathways, typically through 2- (Eqs. 5), 3- (Eq. 6), or 4-electron transfers (Eq. 7), where the selectivity of the 2-electron pathway is particularly desirable for generating H_2O_2 . The challenge lies in ensuring that the cathode material can effectively promote the 2e^- ORR pathway, while minimizing the 4e^- route that leads to water production, thereby improving both the yield and selectivity of H_2O_2 generation.



To achieve this, the design of cathode materials must focus on optimizing their catalytic activity, stability, and conductivity [25]. A

critical strategy involves supporting the catalytic sites on solid substrates to facilitate heterogeneous reactions, thus preventing iron leaching and extending the operational pH range. Solid supports not only stabilize the catalytic components but also enhance electron transfer processes, which are crucial for the efficient cycling of Fe^{3+} and Fe^{2+} in the Fenton reaction. Materials such as mesoporous silica [26], clay [27] and porous carbon [28,29] have been extensively studied as potential supports due to their ability to immobilize iron species and prevent the dissolution of active components, reducing the generation of iron sludge while maintaining catalytic activity over extended periods.

Specifically, carbon materials have gained prominence in recent years as cathode materials for the ORR due to their low cost, stability, high surface area, resistance to acid corrosion and excellent electrical conductivity. These carbon-based electrocatalysts have demonstrated high selectivity for H_2O_2 production; however, their slow reaction kinetics hinder overall efficiency, leading to suboptimal performance. Graphene oxide [30], reduced graphene oxide [31], mesoporous carbon [32], carbon felt [33], activated carbon [34] and carbon aerogels [35, 36] shown promise as catalytic solid supports, though their inherent catalytic activity often falls short when compared to traditional catalysts like platinum (Pt), palladium (Pd), gold (Au) or silver (Ag). Although carbon-based electrocatalysts are highly effective cathodes for ORR and capable of generating H_2O_2 with good selectivity, a key limitation remains: the need to introduce a Fenton catalyst to complete the degradation process. While these carbon materials excel at producing hydrogen peroxide, they lack the intrinsic ability to catalyze the subsequent Fenton reaction, which requires Fenton active species to convert H_2O_2 into $\bullet\text{OH}$ for effective pollutant breakdown. Consequently, the system's reliance on external Fenton catalysts reduces operational efficiency and complicates the process.

To address this, heteroatom doping has emerged as a key modification strategy. The introduction of elements such as nitrogen (N), boron (B), sulphur (S), phosphorus (P), and fluorine (F) into the carbon lattice alters the electronic properties of the material, creating more active sites for the 2e^- ORR, thereby improving the selectivity towards H_2O_2 production [37–43]. Additionally, the diverse heteroatoms species incorporated into the carbon structure contribute to the reduction of H_2O_2 to $\bullet\text{OH}$, further enhancing the overall catalytic efficiency of the system. Alternatively, doping carbon-based materials with transition metals, such as manganese (Mn), copper (Cu), iron (Fe), cerium (Ce), nickel (Ni), and cobalt (Co), has shown notable improvements in the ORR activity, while also providing active sites for Fenton catalysis capable of producing $\bullet\text{OH}$ from H_2O_2 [44–49]. Although transition metals alone tend to catalyze the ORR via the four-electron pathway, leading to direct water formation, their integration into carbon matrices promotes the two-electron pathway. This shift enhances the electrochemical performance by promoting the H_2O_2 production, which is crucial for the Fenton reaction, thus enabling the material to function as both an efficient ORR catalyst and a Fenton catalyst for pollutant degradation.

Therefore, the strategies discussed above pave the way for the development of bifunctional heterogeneous catalysts, capable of simultaneously carrying out the ORR and the Fenton process within a single material [50,51]. This dual functionality not only enhances the overall electrochemical performance but also simplifies the process, reducing the need for separate catalytic systems. Ideally, such catalysts would enable the generation of $\bullet\text{OH}$ directly from oxygen via a 3e^- ORR pathway, by passing the need for H_2O_2 as an intermediate. This would not only streamline the process but also enhance the degradation efficiency of contaminants by directly producing $\bullet\text{OH}$ radicals from O_2 electroreduction.

Designing catalysts that can selectively perform these dual functions remains a challenge, but advances in carbon-based materials and heteroatom/metal doping hold promise for future developments in more efficient and sustainable wastewater treatment technologies. In recent years, our research group has made significant progress in developing bifunctional heterogeneous catalysts for the electro-Fenton process

aimed at antibiotic degradation, with a particular focus on carbon xerogels. These materials are known for their high porosity, tunable surface chemistry, and large surface area, which make them ideal for supporting both the ORR and Fenton catalysis, crucial for pollutant degradation. Initially, we synthesized bifunctional electrocatalysts by doping carbon microspheres with eco-graphene, enabling TC

degradation of up to 83 % via a 3-electron pathway without additional Fenton catalysts [52]. In a subsequent study, we developed Fe-doped carbon xerogels that enhanced ORR performance through the 2-electron pathway and acted as Fenton catalysts, achieving nearly complete degradation of TC at 95.13 % [53]. The third study involved metal-free carbon xerogel-based ORR electrocatalysts inks doped with graphene

(1) Synthesis of manganese microspheres (Mn100)



(2) Synthesis of carbon-coated manganese spheres (C_xMn_y)

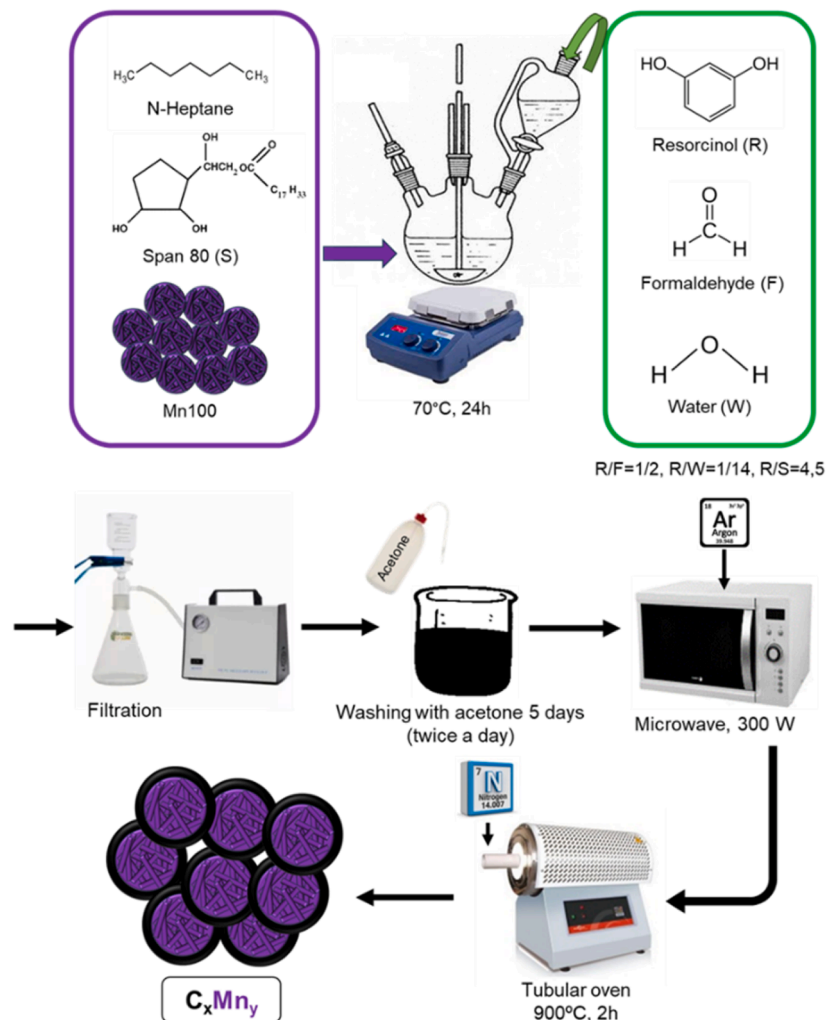


Fig. 1. Synthesis procedure for the preparation of carbon-coated manganese microspheres.

oxide, achieving 90 % amoxicillin degradation through a similar mechanism involving the production of H_2O_2 and subsequent generation of $\bullet\text{OH}$ using a magnetite-coated carbon catalyst ($\text{Fe}_3\text{O}_4/\text{C}$) [54]. Most recently, nitrogen- and eco-graphene co-doped carbon xerogel spheres were synthesized, which also relied on this H_2O_2 -based mechanism, showing improved degradation efficiency for pollutants, ranging from 48 % to 61 %, depending on the nitrogenous groups present [55].

Earlier this year, our research group reported a significant study on the doping of activated biocarbons with manganese, specifically focusing on MnO_x species generated within the carbon structure, which are particularly promising for bifunctional heterogeneous electro-Fenton processes [56]. A 3-electron ORR pathway was proposed, directly producing highly reactive $\text{OH}\bullet$ without the need for an external Fenton catalyst. This approach demonstrated impressive results, achieving up to 70 % TC removal under neutral pH conditions, highlighting the catalytic efficiency of Mn-doped carbon in environmental remediation.

Considering these precedents, the present study introduces a highly innovative synthesis strategy involving the preparation of manganese microspheres coated with carbon xerogel in varying proportions for application as bifunctional electro-Fenton catalysts for TC degradation. This novel core-shell design is expected to allow the carbon matrix to efficiently adsorb the pollutant and enhance electron transfer, while MnO_x particles act as efficient catalytic sites for both the ORR and Fenton processes, leading to the effective TC removal in aqueous solution.

2. Materials and methods

2.1. Materials

Potassium permanganate (KMnO_4 , ≥ 99.0 %, Sigma-Aldrich), manganese (II) sulphate monohydrate ($\text{MnSO}_4 \cdot \text{H}_2\text{O}$, ≥ 99 %, Sigma-Aldrich), resorcinol (99 %, Alfa Aesar), formaldehyde (37 %, Sigma-Aldrich), *n*-heptane (99.8 %, VWR), Span 80 (Sigma-Aldrich), acetone (≥ 99 %, Sigma-Aldrich).

2.2. Synthesis of carbon-coated manganese microspheres

A schematic representation of the experimental procedure used for the synthesis of carbon-coated manganese microspheres is presented in Fig. 1. Manganese ($\text{Mn}100$) microspheres were prepared from KMnO_4 by sonication in an aqueous solution of MnSO_4 . The resulting microspheres were filtered, washed with deionized water until the wash water reached a neutral pH, and then dried in an oven at 140 °C for 24 h. For the subsequent carbon coating, *n*-heptane (900 mL), Span 80 (S), and the previously synthesized Mn microspheres were added to a round-bottom flask equipped with vertical stirring (450 rpm). The mixture was heated to 70 °C, and resorcinol (R), formaldehyde (F), and water (W) were gradually added as carbon precursors. The reaction was maintained under continuous stirring for 24 h under reflux, producing carbon xerogel coating through inverse-emulsion sol-gel polymerization of resorcinol and formaldehyde in the organic solution, as described in previous studies [57]. The molar ratios of the reactants were as follows: $R/F = 1/2$, $R/W = 1/14$, and $R/S = 4.5$. The resulting gel was filtered and immersed in acetone for 5 days, with the acetone being replaced twice daily, to remove residual water and Span 80 from the pores. The material was then filtered again and dried using microwave heating (Saiwod MS-287W microwave oven) in an inert atmosphere (1-min intervals at 300 W) until a constant weight was achieved. Finally, the dried material was carbonized in a nitrogen atmosphere (N_2 flow rate of 300 cm^3/min) at a heating rate of 1 °C/min to a final temperature of 900 °C for 2 h. The carbon-coated microspheres were labeled as CXMnY, where X represents the carbon content and Y represents the theoretical Mn proportion. In addition, a pure carbon spheres sample (C100) was prepared by an analogous synthesis procedure and was used as reference

material [58].

2.3. Textural, chemical and morphological characterization

The textural properties of the samples were evaluated using N_2 adsorption-desorption isotherms at -196 °C. Prior to analysis, the samples were degassed overnight at 110 °C under vacuum conditions (10^{-6} mbar) to eliminate any residual adsorbed gases or impurities. The specific surface area (S_{BET}), micropore volume (W_0), and pore width (L_0) of the samples were determined using the Brunauer-Emmett-Teller (BET) method, the Dubinin-Radushkevich (DR) equation, and Density Functional Theory (DFT), respectively. The mesopore volume was calculated as the difference between the amount of N_2 adsorbed at a relative pressure of 0.95 ($V_{0.95}$) and the micropore volume. Thermogravimetric experiments were performed using a TA Instruments Waters Discovery TGA 550 equipped with a Tru-Mass™ balance, an Evolved Gas Analysis (EGA) furnace and a 25-position autosampler. The samples (10 mg) were placed in Al_2O_3 pans and heated up from 40 °C to 900 °C in 100 mL/min of synthetic air. The crystallinity of the CXMnY samples was assessed using X-ray diffraction (XRD) on a Bruker D8 Advance diffractometer with $\text{Cu K}\alpha$ radiation. Surface chemistry was analyzed by X-ray photoelectron spectroscopy (XPS) using an Escalab 200 R system (VG Scientific Co.) equipped with a $\text{Mg K}\alpha$ X-ray source ($h\nu = 1253.6$ eV) and a hemispherical electron analyzer. The binding energy of the C1s peak at 284.6 eV was used as a reference for identifying other peaks. XPS spectra were fitted by least-squares minimization using Gaussian-Lorentzian peak shapes and a Shirley-type background. The morphology was examined by scanning electron microscopy (SEM) using a LEO (Carl Zeiss) GEMINI-1530 microscope, and by optical microscopy using an OLYMPUS BX51 microscope. Inductively Coupled Plasma Optical Emission Spectroscopy (ICP-OES) analysis was conducted using a PERKIN-ELMER OPTIMA 8300 ICP-OES spectrometer with dual-view capability. The instrument was equipped with a PERKIN-ELMER S10 autosampler for automated sample introduction. Toxicity assessments of the solutions were conducted following the standardized biotest protocol for luminescence inhibition in *Vibrio fischeri* bacteria (UNE/EN/ISO 11345-2), both before and after the electro-Fenton reaction. The LUMISTox 300 System (Dr. Lange GmbH) was employed in conjunction with a LUMISTherm incubator. Toxicity levels were determined by measuring the percentage inhibition at 15 and 30 min of exposure, using a saline stock solution as the control reference.

2.4. Electrochemical characterization

The carbon-coated manganese microspheres samples were tested as cathodic electrodes in the ORR. The oxygen reduction electrochemical performance was evaluated using a Metrohm Autolab PGSTAT101 electrochemical system with a rotating ring-disk electrode (RRDE) setup.

For the preparation of the RRDE, a solution consisting of 1 mL of Nafion and 9 mL of deionized water was prepared and then sonicated for 10 min. From this solution, 1 mL was extracted and mixed with 5 mg of CXMnY, followed by an additional 30 min of sonication. A 20 μL aliquot of the final ink was deposited onto the RRDE and allowed to dry for 10 min under infrared radiation.

Measurements were conducted in a standard three-electrode cell at ambient temperature, using a platinum plate as the counter electrode and an Ag/AgCl electrode as the reference. The electrolyte was a 0.1 M KOH solution prepared with deionized water. Prior to each measurement, the electrolyte was saturated with either N_2 or O_2 by bubbling the desired gas into the 0.1 M KOH solution for 30 min at room temperature.

Cyclic voltammetry (CV) was performed in the potential range of 0.40 V to -0.80 V (vs. Ag/AgCl), at a sweeping potential rate of 50 mV s^{-1} with the electrode rotating at 1000 rpm, in both N_2 - and O_2 -saturated solutions.

Linear sweep voltammetry (LSV) for ORR was carried out across the

same potential range at a scan rate of 50 mV s^{-1} , with the electrode rotation speed varied between 500 and 3500 rpm (increments of 500 rpm). The number of electrons transferred and the H_2O_2 selectivity were calculated from the RRDE data using Eqs. (8) and (9), as described in references [59,60]:

$$n = \frac{4 \times I_D}{I_D + \frac{I_R}{N}} \quad (8)$$

$$\% \text{H}_2\text{O}_2 = 100 \times \frac{2 \times \frac{I_R}{N}}{I_D - \frac{I_R}{N}} \quad (9)$$

where I_D and I_R represent the disk and ring currents, respectively, and N is the collection efficiency of the RRDE (0.249).

The Koutecky–Levich model (Eq. 10) was applied to fit the LSV data in order to investigate the electron transfer mechanism and kinetics at the electrode, allowing for the determination of the number of electrons transferred (n) and the kinetic current density (J_K):

$$\frac{1}{J} = \frac{1}{J_K} + \frac{1}{B \times \omega^{1/2}} \quad (10)$$

Where ω is the rotation speed and B is given by Eq. (11):

$$B = (0.62) \times n \times F \times A \times D^{2/3} \times \nu^{-1/6} \times C \quad (11)$$

In this equation, F is Faraday's constant (96485 C mol^{-1}), n is the number of electrons transferred per oxygen molecule, A is the RRDE disk area (0.2475 cm^2), D is the oxygen diffusion coefficient ($1.9 \times 10^{-5} \text{ cm}^2 \text{ s}^{-1}$), ν is the kinematic viscosity ($0.01 \text{ cm}^2 \text{ s}^{-1}$), and C represents the oxygen solubility ($1.2 \times 10^{-6} \text{ mol cm}^{-3}$) [61,62].

2.5. Electro-Fenton process

The Electro-Fenton process was carried out in order to evaluate the dual-functional electrocatalytic activity of the CXMnY samples. The EF reaction was conducted in a three-electrode electrochemical cell with a solution capacity of 150 mL at room temperature. TC at an initial concentration of 40 mg/L was selected as the target pollutant, and sodium sulfate (Na_2SO_4 , 0.5 M) was used as the supporting electrolyte. The working electrode was fabricated by mixing 45 mg of CXMnY with 8.5 mg of polytetrafluoroethylene (PTFE, 60 % dispersion) in a mass ratio of 9:1 to form a homogeneous paste. This paste was dried at 100°C for 12 h, and 50 mg of the dried material was applied to both sides of a graphite sheet ($2.5 \text{ cm} \times 1 \text{ cm}$). The reference electrode was Ag/AgCl, and a platinum wire served as the counter electrode. The electrochemical system was controlled using a Biologic VMP multichannel potentiostat, with the applied potential fixed at -0.6 V throughout the experiment.

To ensure that any adsorption of TC onto the materials was negligible, the electrodes were pre-saturated in the dark for 24 h in the electrolyte solution ($0.5 \text{ M Na}_2\text{SO}_4/\text{TC}$) before the EF tests. The initial concentration of TC was monitored using UV-Vis spectrophotometry at a wavelength of 357 nm with a Shimadzu UV-2600i spectrophotometer. Once the EF experiment began, oxygen gas was bubbled into the solution for 30 min before applying the voltage, and the bubbling continued throughout the experiment to maintain oxygen saturation.

During the EF process, 1 mL aliquots of the solution were periodically withdrawn from the cell at regular intervals, and the concentration of TC in each aliquot was immediately analyzed by UV-Vis spectrophotometry. The working pH was maintained at 6.5, corresponding to the natural pH of the TC solution.

3. Results and discussion

3.1. Textural, structural, morphological and chemical surface characterization

A detailed morphological analysis of the manganese-carbon xerogel composites was provided by SEM images at different magnification (Fig. 2), showing distinct surface characteristics that reflect the effectiveness of carbon xerogel coating on the manganese microspheres. The Mn100 sample, composed entirely of manganese, exhibited microspheres approximately $1.8 \mu\text{m}$ in diameter, with a densely packed surface populated by nanoscale rods or nanorods, typically observed for the well-defined crystalline phase $\gamma\text{-MnO}_2$ [63]. In the carbon-coated samples (C10Mn90, C50Mn50, C70Mn30, C80Mn20, and C90Mn10), the SEM images reveal a significant transformation in surface morphology compared to the Mn100 sample. Unlike Mn100, where individual nanorods are clearly visible, the carbon-coated composites show uniformly porous surfaces without visible nanorod structures. This change in surface texture indicates the successful encapsulation of manganese microspheres by the carbon xerogel, forming a continuous and homogeneous carbon layer around each microsphere. The porous and conductive nature of this carbon layer could act as a protective barrier isolating the manganese core from the reaction medium, as well as improve the surface area, reactant access and electron transfer. As a reference, the C100 sample, which consists solely of carbon xerogel, displays microspheres with a significantly larger diameter (approximately $18\text{--}20 \mu\text{m}$). The morphology is characterized by a highly porous, homogeneous structure, which is typical of carbon xerogels [64]. This porous network maximizes surface area and provides numerous adsorption sites, making it suitable for electrochemical applications.

Textural properties of the CXMnY samples were analyzed by N_2 adsorption-desorption isotherms (Fig. 3). All materials exhibited a combination of type I and IV isotherms, suggesting the presence of both microporous and mesoporous structures, as typically seen in carbon xerogels [64], with a slight contribution of macropores. Specifically, at low relative pressures ($P/P_0 < 0.1$), there is a noticeable N_2 adsorption that corresponds to micropore filling. At intermediate pressures ($P/P_0 = 0.4\text{--}0.9$), the appearance of a hysteresis loop indicates the presence of mesopores. Such behavior suggests that these materials are suitable for adsorption-based applications, as they combine the advantages of high surface areas from microporosity and larger pore structures from mesoporosity. The presence of macropores is minimal, as indicated by the sharp increase in N_2 adsorption at higher relative pressures ($P/P_0 > 0.9$), which is more pronounced in samples with higher manganese content (e.g., C10Mn90). The observed hysteresis loop in the isotherms is characteristic of H4-type hysteresis, which is typical of materials that contain slit-like pores or plate-like particles. This further supports the mesoporous nature of the carbon xerogels, where the mesopores likely arise from interparticle voids and the structural defects created during synthesis, particularly with the addition of MnO_x . This mesoporous nature allows for enhanced diffusion of molecules into the bulk of the material, which is advantageous for catalytic applications such as ORR and electro-Fenton processes.

The porous characteristics of the samples, as summarized in the Table 1, show important trends. The BET surface area (S_{BET}) and DFT mesoporous surface area (S_{DFT}) for the pure carbon xerogel sample (C100) are 589 and $715 \text{ m}^2/\text{g}$, respectively, indicating a well-developed porosity. As manganese is introduced, the surface area first increases slightly for C90Mn10 ($626 \text{ m}^2/\text{g}$) but decreases for samples with higher Mn content (down to $341 \text{ m}^2/\text{g}$ for C10Mn90). The initial increase in surface area for C90Mn10 can be attributed to the incorporation of manganese, which may generate additional surface defects that increase surface area. However, as the Mn content increases, the surface area decreases, likely due to the blockage of micropores by MnO_x particles, which are relatively large compared to the pore structure of the carbon matrix. This trend is consistent with the literature, where increased

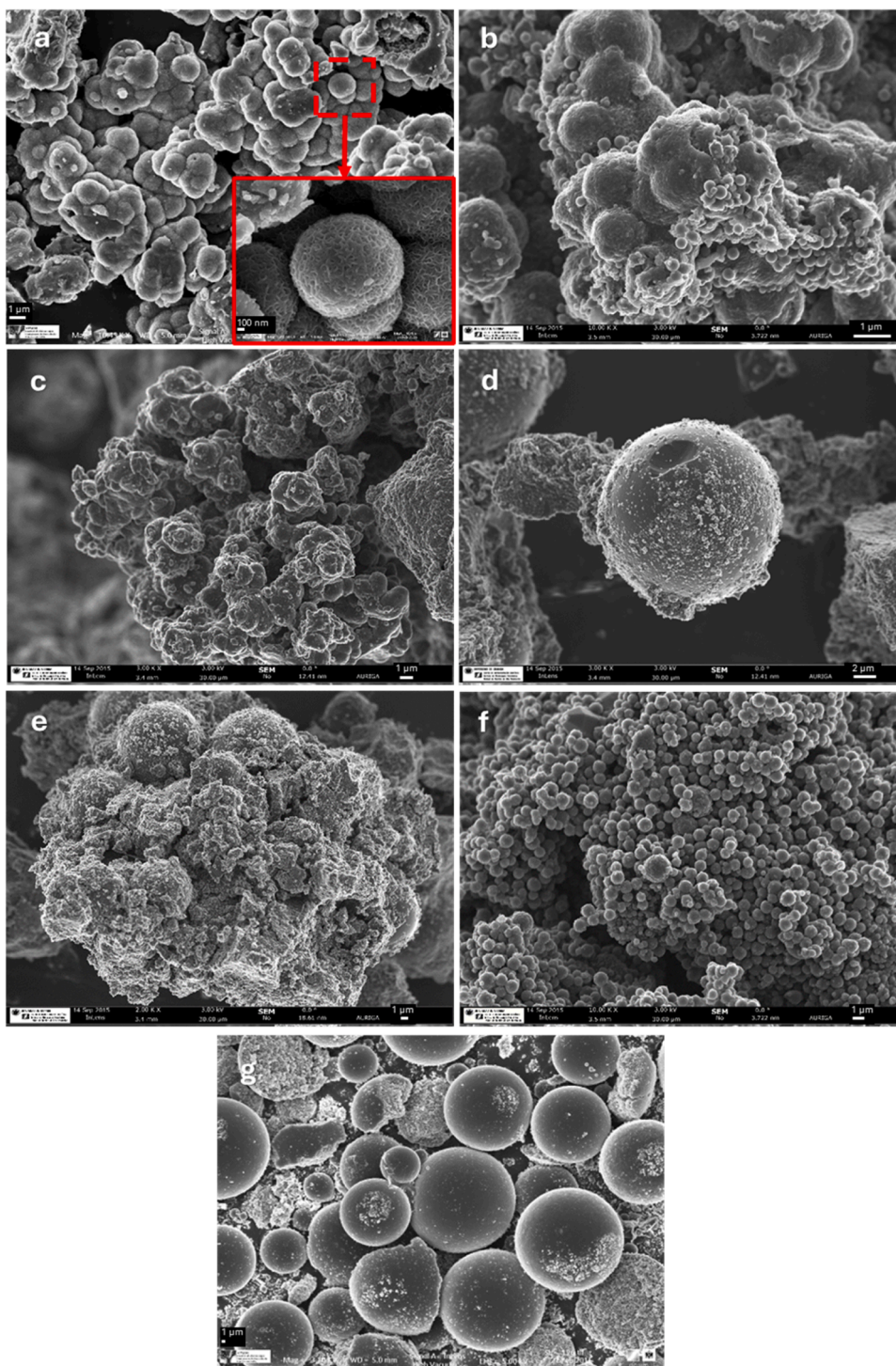


Fig. 2. SEM images of a) Mn100, b) C90Mn10, c) C80Mn20, d) C70Mn30, e) C50Mn50, f) C10Mn90, and g) C100.

metal loading leads to a reduction in surface area due to pore blockage [65]. The total pore volume ($V_{0.95}$) follows a similar trend, increasing slightly for C90Mn10 ($0.25 \text{ cm}^3/\text{g}$) compared to C100 ($0.23 \text{ cm}^3/\text{g}$), but decreasing significantly for the highest Mn loading ($0.19 \text{ cm}^3/\text{g}$ for C10Mn90). Mesopore volume (V_{meso}) also shows a reduction with increasing Mn content. For example, the mesopore volume decreases from $0.20 \text{ cm}^3/\text{g}$ for C100 to $0.11 \text{ cm}^3/\text{g}$ for C10Mn90. This suggests that MnO_x primarily occupy the mesopores, leading to a reduction in available pore volume for adsorption. Micropore volume ($W_0(\text{N}_2)$) decreases only slightly with increasing Mn content, indicating that the microporosity is better preserved than mesoporosity. For instance, the

micropore volume drops from $0.23 \text{ cm}^3/\text{g}$ (C100) to $0.19 \text{ cm}^3/\text{g}$ (C10Mn90), suggesting that the microporous structure of the carbon xerogel matrix is less affected by Mn incorporation than the mesoporous structure. Regarding the micropore width ($L_0(\text{N}_2)$), an increase with higher Mn content was observed, rising from 0.57 nm for C100 to 0.95 nm for C10Mn90. This suggests that manganese incorporation causes an enlargement of micropores, likely due to pore expansion or destruction of smaller pores as MnO_x particles occupy and modify the porous structure. The increase in micropore width further supports the hypothesis that MnO_x are deposited inside the carbon matrix, enlarging the pore diameter while blocking smaller pores. This change in pore size

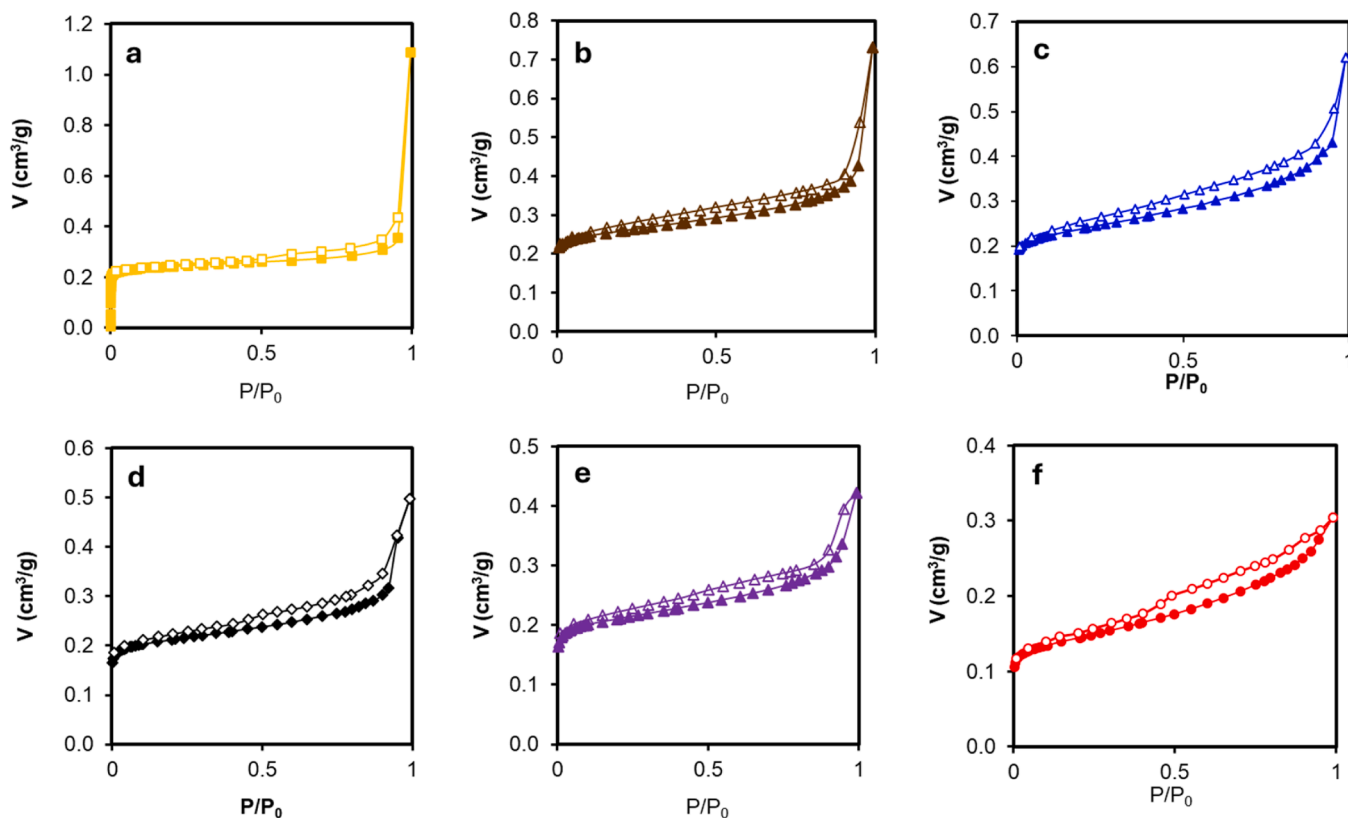


Fig. 3. N_2 adsorption-desorption isotherms at $-196\text{ }^\circ\text{C}$ of pure C100, pure Mn100 and CXMnY samples.

Table 1

Porous textural properties of pure C100 and CXMnY samples.

Sample	S_{BET} (m^2/g)	S_{DFT} (m^2/g)	$W_0(N_2)$ (cm^3/g)	$L_0(N_2)$ (nm)	$V_{0.95}$ (cm^3/g)	V_{meso} (cm^3/g)
C100	589	715	0.23	0.57	0.43	0.20
C90Mn10	626	694	0.25	0.80	0.43	0.18
C80Mn20	513	563	0.24	0.83	0.42	0.18
C70Mn30	517	564	0.25	0.82	0.42	0.17
C50Mn50	570	680	0.31	0.77	0.43	0.12
C10Mn90	341	381	0.19	0.95	0.30	0.11

distribution is critical for catalytic applications where both micropores and mesopores contribute to the overall performance. Therefore, among the CXMnY materials, C90Mn10 presented particularly promising textural characteristics for electrocatalytic applications. This sample had the highest S_{BET} , S_{DFT} and micro-/mesopore volume, which are critical factors for enhancing the bifunctional electro-Fenton performance. The microporosity will promote the adsorption of contaminants like TC, while the mesopores and total pore volume will support efficient mass and electron transport during electrocatalysis [66,67].

The TGA analysis in Figure S1 provides insights into the thermal stability and inorganic composition of carbon-coated manganese microspheres. The TGA curves thus reflect both the decomposition of the carbon xerogel coating and the thermal stability of the manganese oxide cores [56]. The TGA data reveal that C100, which consists solely of carbon xerogel without any manganese, exhibits a very low residual mass (0.5%), consistent with the absence of inorganic content. In contrast, samples with increasing theoretical manganese content (C90Mn10 to Mn100) display progressively higher residual masses, which correlate with the presence of manganese oxide after combustion of the organic carbon xerogel layer. For samples up to C70Mn30, the experimentally determined percentages of residual inorganic mass align closely with theoretical predictions (C90Mn10: 12.9%, C80Mn20:

19.3%, and C70Mn30: 24.6%). This close match suggests that the synthesis approach effectively coats the manganese microspheres with a consistent layer of carbon xerogel up to this manganese content, confirming the homogeneity of the carbon coating on the manganese spheres at lower manganese loadings. However, for composites with manganese contents of 50% or more (C50Mn50, C10Mn90, and Mn100), significant deviations arise between theoretical and experimental inorganic content. For example, the residual inorganic content in C50Mn50, C10Mn90, and Mn100 reaches 81.9%, 84.1%, and 83.8%, respectively; values much higher than expected. These findings indicate an excessive accumulation of manganese oxide and suggest that, in these high-manganese samples, the carbon xerogel does not fully or uniformly coat the microspheres, possibly due to synthesis challenges introduced at high manganese concentrations. A likely explanation for this phenomenon is that the large amount of manganese microspheres disrupts the resorcinol-formaldehyde polymerization process, which forms the carbon xerogel layer. In these cases, the manganese particles may aggregate and form clusters, reducing the effectiveness of carbon xerogel coating formation. Consequently, instead of a uniform coating, there may be exposed manganese oxide surfaces and partial or non-uniform carbon coverage. This incomplete coating leads to a lower-than-expected organic fraction and a higher residual manganese oxide content upon TGA analysis. On the other hand, manganese oxides can act as catalysts for the oxidative decomposition of carbon. In samples with high manganese content, the manganese oxide core may catalyze the thermal decomposition of the carbon xerogel coating at a lower temperature, resulting in accelerated weight loss of the carbon phase and a higher residual manganese oxide fraction. Additionally, high concentrations of manganese might also lead to phase transformations within the manganese oxide core. Different manganese oxide phases exhibit varied thermal stabilities, and such transformations could lead to unexpected weight loss or retention patterns in TGA, further contributing to deviations in inorganic content.

The structural characterization of the synthesized materials, as

depicted by the X-ray diffraction (XRD) patterns (Fig. 4), reveals distinct crystalline phases and provides insights into the compositional and functional properties of the samples. The XRD pattern for C100, representing the 100 % carbon xerogel, showed broad, low-intensity peaks characteristic of amorphous carbon located at 2θ values around 25° and 44° , corresponding to the (002) and (100) planes of graphite, in accordance with JCPDS card No. 89–8487, as indicated by the square symbols in the diffractogram [68]. The absence of sharp peaks underscores the lack of long-range crystalline order, demonstrating that these carbon xerogels possess a high concentration of graphitic clusters. While amorphous carbon contributes limited catalytic activity directly, the structure of these carbon xerogel microspheres provides several critical benefits for electrochemical applications. Generally, carbon xerogels demonstrate elevated capacitance that enhances their ability to sustain electron flow, which is crucial for stable ORR performance, while also delivering notable current density that amplifies overall reaction rates [69]. Moreover, these materials have shown a strong preference for a two-electron ORR pathway [55], selectively generating H_2O_2 rather than fully reducing O_2 to H_2O , which is advantageous for the electro-Fenton process. The Mn100 sample, consisting entirely of manganese, exhibited sharp diffraction peaks at 22° , 37° , 42° , 55° and 66° related to the planes (120), (131), (300), (160) and (421), respectively, that align with $\gamma\text{-MnO}_2$ (gamma manganese dioxide) corresponding to JCPDS card No. 14–0644 [70,71]. This phase preferably favors the 4-electron pathway in ORR, directly reducing O_2 to H_2O , which enhances efficiency by minimizing intermediate peroxide formation [72]. On the other hand, the carbon-coated manganese microspheres (C90Mn10, C80Mn20, C70Mn30, C50Mn50, and C10Mn90) exhibited XRD patterns indicative of a composite structure, with contributions from both amorphous carbon and crystalline manganese oxide phases. This combination of phases suggests that the carbon xerogel coating effectively encapsulates the manganese microspheres, creating a hybrid material with desirable catalytic properties. Among the crystalline manganese oxides, MnO (manganese (II) oxide) and Mn_3O_4 (a mixed-valence spinel phase with Mn^{2+} and Mn^{3+} ions) were distinctly observed. MnO was identifiable by triangular reflections corresponding to JCPDS card No. 07–0230 at 35° , 41° , 59° , 70° and 74° attributed to the planes (111), (200), (220), (311) and (222), respectively, indicating its presence as a well-defined crystalline phase [73]. Meanwhile, Mn_3O_4 was characterized by black circular peaks in the XRD pattern at 18° , 29° , 31° , 32° , 36° , 38° , 44° , 50° , 60° , and 64° associated with the planes (101), (112), (200), (103), (211), (004), (220), (105), (224), and (400), respectively, aligning with JCPDS card No. 24–0734, which confirmed the formation of this spinel structure [73,74]. Each manganese oxide phase plays a unique role in

the catalytic process: MnO contributes to the Fenton-like activity by providing Mn^{2+} ions, which act as Fenton catalysts for H_2O_2 decomposition, while Mn_3O_4 facilitates a synergistic redox cycle between Mn^{2+} and Mn^{3+} , enhancing the ORR and supporting the bifunctional catalytic performance of the material. This dual-phase configuration, supported by the conductive carbon matrix, optimizes the system for both ORR and Fenton reactions, thus proving highly effective for applications in the electro-Fenton degradation of pollutants.

The surface chemical composition of the samples was investigated using XPS technique, as shown in Fig. 5, which presents the spectra for C_{1s} , O_{1s} , and Mn_{2p} signals. From the deconvolution of these spectra, the surface elemental composition was quantified, and the results were summarized in Table S1. Variations in the relative percentages of C, O and Mn with increasing carbon were revealed. In particular, the data demonstrated a clear trend: as the proportion of carbon coating increased across the series of samples (from Mn100 to C90Mn10), there was a corresponding increase in the weight percentage of carbon (%wt C) and a notable decrease in the weight percentages of both oxygen (%wt O) and manganese (%wt Mn). The C100 sample, composed entirely of carbon xerogel, exhibited the highest %wt C (91.6 %) with only minor oxygen content (8.4 %) and no detectable manganese, which is expected given its pure carbon nature. Conversely, the Mn100 sample showed a substantial %wt Mn (37.8 %) and %wt O (62.2 %) with no carbon present. Carbon-coated manganese microsphere sample displayed a decreasing oxygen and manganese content as the carbon percentage in the sample increases. For instance, in C10Mn90, %wt C is 68.0 %, with %wt O and %wt Mn at 20.6 % and 11.4 %, respectively, whilst the C90Mn10 sample contained 92.2 %, 6.23 % and 1.5 % of %wt C, %wt O and %wt Mn, respectively. These findings confirmed that increased carbon xerogel coating effectively encapsulates the manganese oxide core, reducing its exposure and thus its signal in the XPS analysis, while increasing the carbon surface signal.

Regarding the high resolution C_{1s} core-level spectra (Fig. 5a), six distinct peaks were identified and deconvoluted: C=C (284.6 eV), C-C (285.6–285.7 eV), C-O (286.5–286.6 eV), C=O (287.5–288.1 eV), O-C=O (288.8–289.2 eV), and $\pi\text{-}\pi^*$ transitions in the aromatic systems (290.1–290.4 eV), which correspond to sp^2 and sp^3 carbon bonds, as well as various oxidized carbon functionalities [52,53]. These binding energies (BE) and their associated functional groups remained relatively constant across all samples, indicating that the incorporation of manganese did not alter the primary carbon surface chemistry. In the carbon-rich samples, such as C90Mn10, a notable decrease in the full width at half maximum (FWHM) for the C=C peak at 284.6 eV was observed, reaching a minimum of 1.24. This narrowing of FWHM suggests an increase in the crystallinity of the graphitic structure, likely due to the stabilization and alignment of graphitic domains within the carbon xerogel matrix. Such an increase in crystallinity can be associated with enhanced electrical conductivity, which is crucial for optimizing electrode performance. In contrast, as the manganese content increases, the FWHM for the C=C peak broadens, reaching 1.40 in the C10Mn90 sample. This broadening is indicative of a higher defect density within the graphitic structure or a reduction in microcrystal size, both of which can contribute to diminished conductivity. These findings imply that the increased presence of manganese may induce structural disruptions within the graphitic domains as a result of interactions with manganese oxide species, thereby altering the conductive properties of the material.

In the analysis of the O_{1s} region (Fig. 5b), deconvolution revealed distinct peaks associated with different oxygen environments. The oxygen species in the Mn100 sample, which primarily contains $\gamma\text{-MnO}_2$, were classified into three main types [70]: i) lattice oxygen (O_{latt}) at 529.7 eV, associated to oxygen atoms covalently bonded to manganese atoms forming part of its crystalline structure, ii) surface oxygen species (O_{surf}) at 531.8 eV, which can arise from defects or oxygen vacancies on the MnO_2 surface, and iii) adsorbed molecular water ($\text{O}_{\text{H}_2\text{O}}$) at 533.5 eV, which is a feature commonly seen in metal oxides with high surface area, where atmospheric moisture binds to the surface. In the carbon-coated

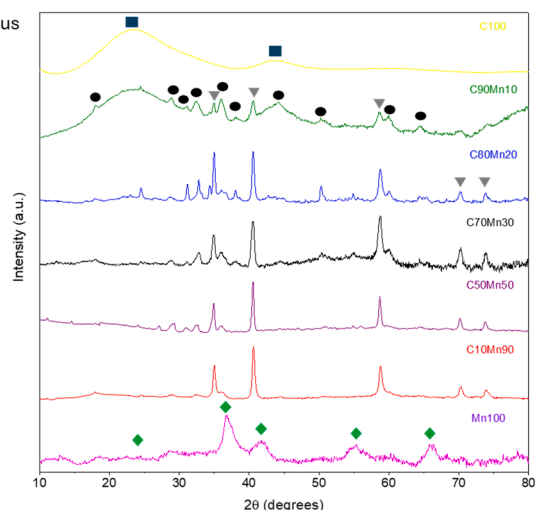


Fig. 4. XRD patterns of pure C100, pure Mn100 and CxMnY samples.

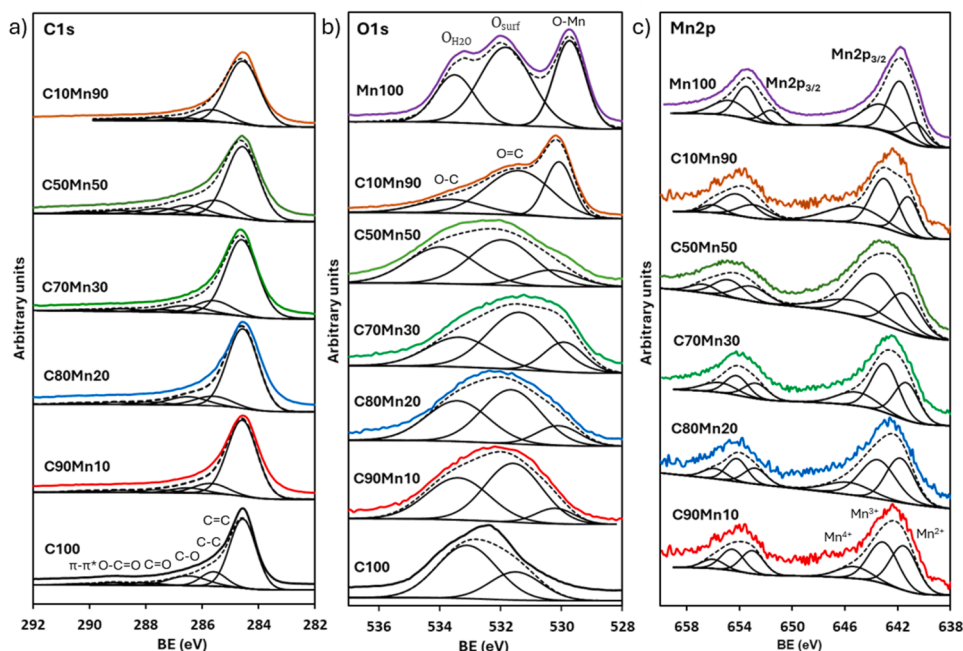


Fig. 5. XPS spectra of a) C1s, b) O1s and c) Mn2p for all samples.

samples (C10Mn90 to C90Mn10), the O1s spectra revealed, in addition to the O-Mn bond (530.1–530.3 eV), the presence of new peaks attributed to the O=C (531.4–531.6 eV) and O-C (533.4–533.9 eV) species resulting from the carbon coating process [56]. As the carbon content increases, the intensity (% peak) of the O-Mn contribution decreases, while the peaks attributed to O=C and O-C bonds become more pronounced. This trend suggests a shift in surface oxygen composition, with a greater proportion of oxygen species associated with carbon functionalities as opposed to manganese oxide. This shift aligns with the successful encapsulation of manganese microspheres in a carbon xerogel matrix, effectively modifying the surface oxygen environment. The C100 sample, which consisted entirely of carbon xerogel, displayed only the O=C and O-C peaks, with no detectable O-Mn contribution, confirming the absence of manganese and the dominance of oxygenated carbon groups on its surface.

Fig. 5c presents the high-resolution Mn_{2p} XPS spectra, which revealed a doublet with three primary peaks in the range of 641.0–646.0 eV and 653.0–659.0 eV corresponding to Mn (2p_{3/2}) and Mn (2p_{1/2}), respectively, as a result of spin-orbit splitting [75]. Consequently, the fitting was conducted solely on the Mn (2p_{3/2}) peak with its respective components. The details regarding the positions, and percentage concentrations of the fitted XPS contributions are presented in Table S1. Therefore, the Mn (2p_{3/2}) spectra for Mn100 was resolved into three distinct species: Mn²⁺, Mn³⁺, and Mn⁴⁺, with BE of 640.6 eV, 641.8 eV, and 643.2 eV, respectively [70]. These species are characteristic of the γ -MnO₂ crystalline phase confirming the results obtained by XRD analysis. The presence of Mn³⁺ and Mn²⁺ species in the XPS spectrum indicates the complexity of the system. This phenomenon may be attributed to structural defects, chemical interactions, and the specific conditions of sample preparation and analysis. The coexistence of different oxidation states of manganese suggests a dynamic equilibrium influenced by the structural integrity of the material and external environmental factors during synthesis and characterization. The percentage contributions were approximately 16 %, 49 %, and 35 % for Mn²⁺, Mn³⁺, and Mn⁴⁺, respectively.

The carbon-coated Mn microspheres samples underwent an evolution of the Mn species depending on the proportions of carbon xerogel and Mn introduced in the synthesis procedure, where the pyrolysis step at 900°C in an inert nitrogen atmosphere could have been critical. High

temperatures lead to the reduction of MnO₂, potentially resulting in the conversion of Mn⁴⁺ to Mn³⁺ and Mn²⁺ [76]. Carbon-based materials have demonstrated efficacy as reducing agents for metal catalysts in various reactions conducted under inert atmosphere, which prevents further oxidation allowing reduction reactions to dominate [77]. Therefore, higher amounts of carbon xerogel coating may facilitate greater reduction of Mn⁴⁺ to Mn²⁺. In the case of lower carbon proportions, Mn⁴⁺ may remain stable, while Mn³⁺ may also be present depending on the initial contributions and the interactions during the coating process. Consequently, the Mn²⁺/Mn³⁺ ratio increases from 0.61 in sample C10Mn90 to 0.97 in C90Mn10, supporting the preceding argument.

3.2. Electrochemical characterization

The cyclic voltammetry (CV) analysis of the synthesized samples, conducted using a rotating ring-disk electrode (RRDE) in a 0.1 M KOH solution under both nitrogen and oxygen atmospheres, is shown in Fig. 6. In the N₂-saturated condition, the CV curves (blue lines) revealed baseline capacitive behaviour for each sample, which provides insights into their textural and conductivity properties. Under O₂ saturation (red lines), the presence of the ORR process can be inferred, particularly for samples with lower Mn content, where the current response is markedly enhanced. For the Mn100 sample, which exhibited minimal current variation in both nitrogen and oxygen environments, the observed low capacitance suggests limited surface area and mesoporosity, attributes that are typically associated with pure manganese oxides and minimal conductive carbon content [78,79]. This limited electrochemical response aligns with the absence of a carbon coating, resulting in a sample that lacks extensive porosity. In contrast, the carbon-coated samples (C10Mn90 through C90Mn10) display increasingly larger enclosed areas in their CVs as the carbon content rises, indicating enhanced capacitance. This increase can be attributed to a higher surface area and mesoporous volume, facilitating the formation of the electrochemical double-layer (ECDL) capacitance [53,80]. The C100 sample, composed entirely of carbon xerogel, exhibits the highest capacitance due to its extensive surface area and mesoporous structure, which enhances electrolyte diffusion and electric double-layer formation. The predominance of carbon also contributes to improved

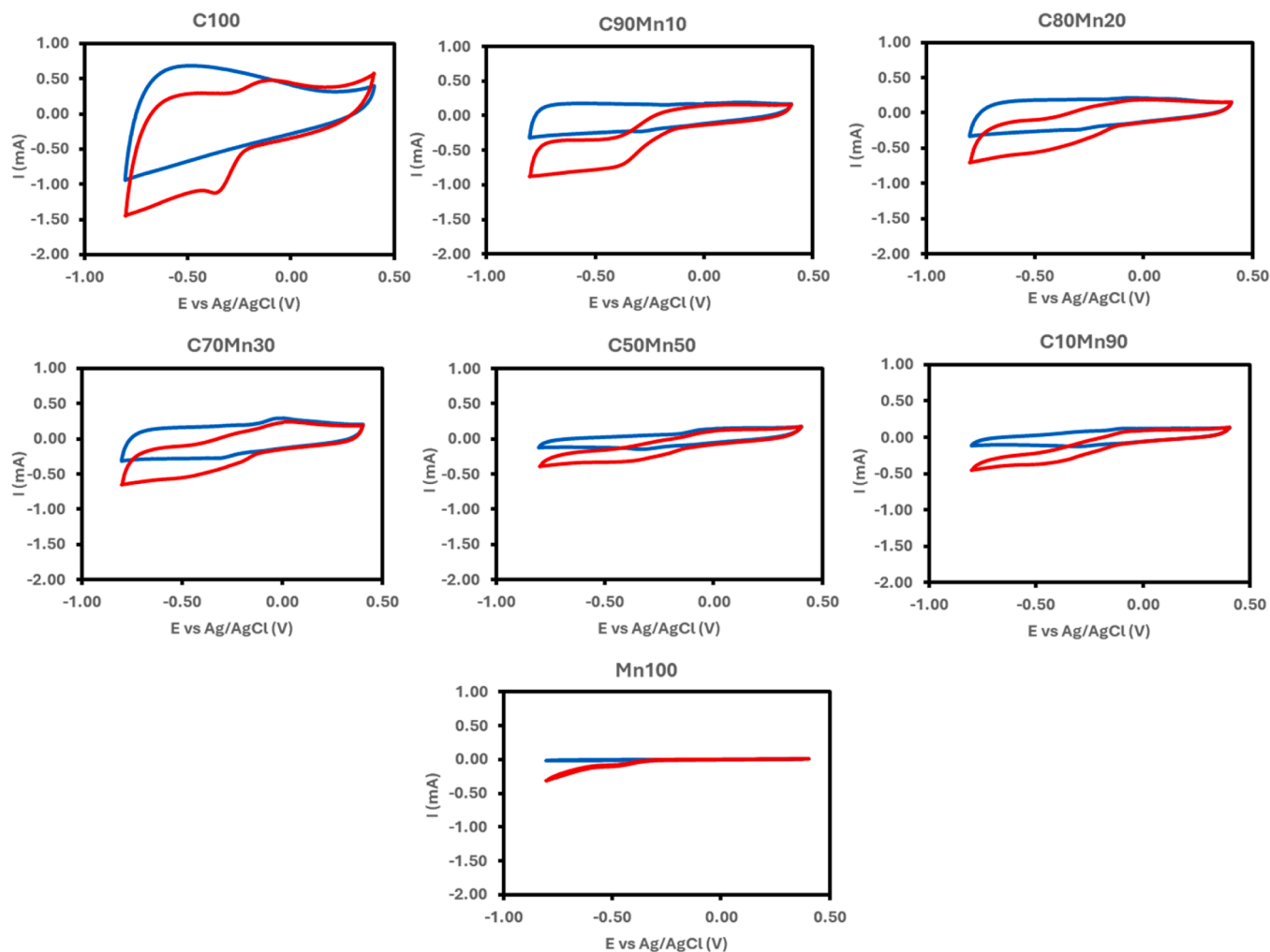


Fig. 6. Cyclic voltammograms at 1000 rpm and 50 mV/s of all samples in N_2 bubbling (blue line) and O_2 bubbling (red line) KOH solution.

conductivity, further enhancing the capacitance. Notably, in the presence of O_2 saturated conditions, the CV profiles show an increase in current density around -0.2 V vs. Ag/AgCl, indicative of ORR activity. This effect is more pronounced in samples with a higher proportion of carbon xerogel, where the conductive matrix allows for better electron transfer and enhances ORR kinetics. This trend suggests that the carbon xerogel coating not only improves capacitance due to an increase in surface area and mesoporosity but also promotes ORR by facilitating electron transport through the conductive carbon network. Among the Mn-coated carbon microspheres, the C90Mn10 sample appeared to exhibit the most optimal characteristics, providing the highest current density and capacitance.

For a more detailed analysis, Linear Sweep Voltammetry (LSV) was performed at various rotation speeds of the RRDE, ranging from 500 to 3500 rpm, for the C90Mn10 sample (Fig. 7a). As anticipated, the current intensity increased with higher rotation speeds due to reduced mass diffusion limitations from 500 rpm to 3500 rpm. Fig. 7b shows the LSV curves for each sample at a rotation speed of 3500 rpm, where a trend of increasing current intensity was observed with a higher carbon xerogel coating, reaching a maximum kinetic current density (J_k) of 9.43 mA cm^{-2} for C90Mn10 at -0.6 V vs. Ag/AgCl (Table 2). The pure carbon xerogel (C100) exhibited a slightly lower current density than C90Mn10, but it remains higher than the other CXMnY samples and the pure manganese oxide sample (Mn100). This behaviour could be attributed to the conductive network and high surface area provided by the carbon xerogel. However, the lack of Mn-related catalytic sites in

C100 may limit its ORR activity compared to C90Mn10, where the synergy between carbon and manganese enhances the electrocatalytic performance. Conversely, Mn100, having no carbon coating, demonstrated significantly lower current density due to the limited surface area and mesoporosity and conductivity for effective ion diffusion. Figs. 7c and 7d illustrate the evolution of the number of electrons transferred (n) and H_2O_2 selectivity over the potential range from -0.4 to -0.8 V for all samples, as calculated from the RRDE data. The n values provided insights into the mechanism of the ORR. For a fully efficient ORR pathway, ideally involving four electrons, O_2 is directly reduced to water H_2O , which is desirable for applications like rechargeable metal-air batteries, water splitting or reversible fuel cells [81]. The Mn100 sample, as expected for MnO_2 -based materials [72], primarily directed the ORR through a four-electron ($4e^-$) pathway, efficiently reducing O_2 to H_2O . This characteristic makes MnO_2 an effective catalyst for complete ORR applications where water production is targeted. In contrast, the C100 sample also aligned with anticipated behaviour for carbon xerogels, favouring a two-electron ($2e^-$) route that produces H_2O_2 as the main reduction product [55]. This is typical for carbon-based materials, as they generally promote a less complete reduction process due to their limited catalytic sites for ORR. Interestingly, by increasing the carbon xerogel coating on the manganese microspheres, we observe a gradual shift toward an intermediate pathway with approximately three electrons ($3e^-$) transferred. This intermediate behaviour suggests the possibility of generating $\bullet OH$ directly, which is advantageous in applications like bifunctional electro-Fenton reactions [56], where the formation of

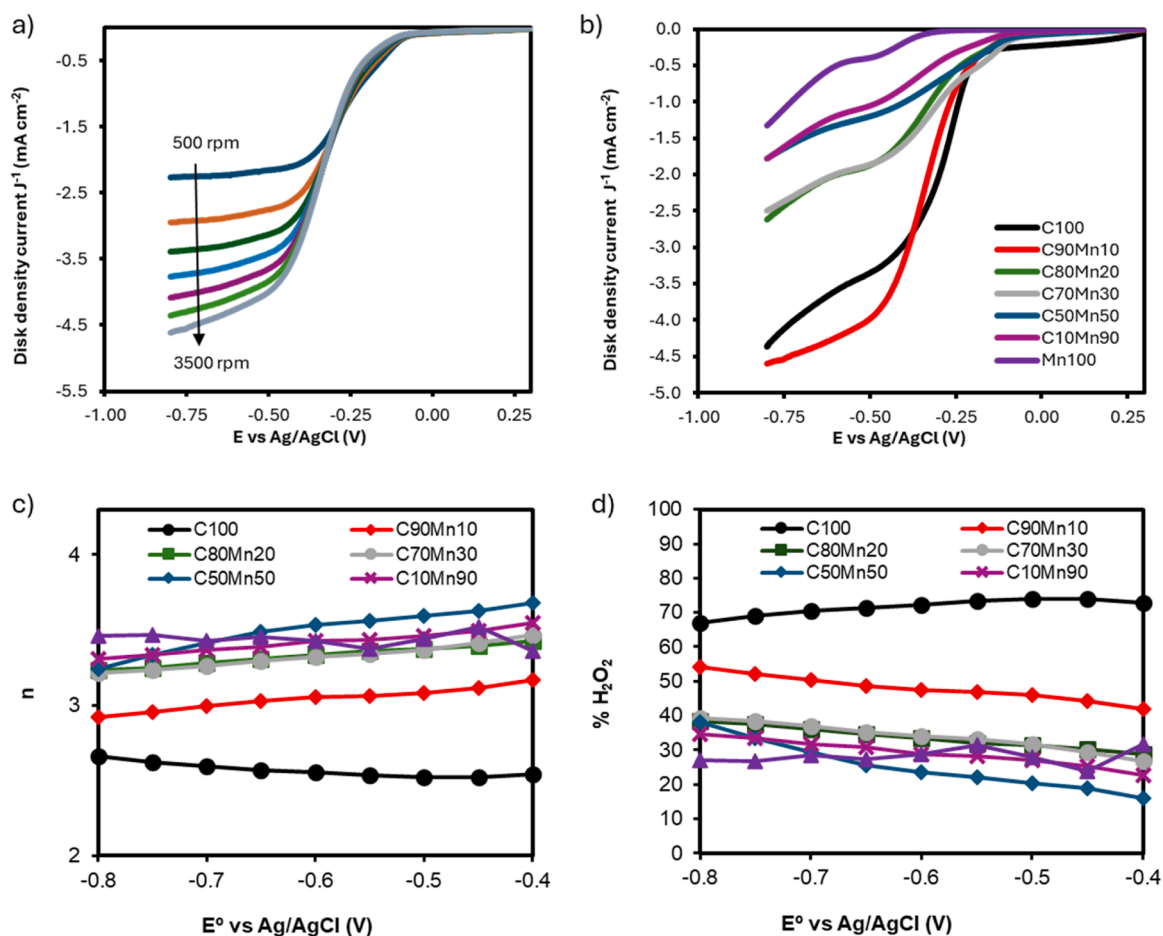


Fig. 7. a) LSV curves for C90Mn10 sample at different RRDE rates, and b) all samples at 3500 rpm (b). c) number of electrons transferred, and d) the % H₂O₂ produced at each potential from -0.4 V to -0.8 V for all samples.

Table 2

Electrochemical parameters obtained from the LSV curves: onset potential (E_{onset}), number of electrons transferred (n), and kinetic current density (J_K).

Sample	E_{onset}	J_K (mA cm ⁻²) at -0.6 V (vs. Ag/AgCl)	n at -0.6 V (vs. Ag/AgCl)
C100	-0.18	6.74	2.55
C90Mn10	-0.18	9.43	3.05
C80Mn20	-0.11	2.75	3.33
C70Mn30	-0.09	2.67	3.32
C50Mn50	-0.12	1.63	3.53
C10Mn90	-0.13	1.39	3.42
Mn100	-0.3	0.5	3.42

reactive oxygen species such as $\bullet\text{OH}$ is desirable for pollutant degradation and other advanced oxidation processes. These results are consistent with findings from XRD and XPS analyses, which provide complementary evidence of the material composition and surface characteristics. XRD confirmed the presence and structural integrity of MnO_x phases, while XPS data supported the interaction between carbon xerogel and manganese, potentially enhancing the electron transfer efficiency and adjusting the ORR pathway depending on the carbon coating content. Regarding H₂O₂ generation, the highest selectivity among the CXMnY samples was observed for C90Mn10, reaching over 50 % at -0.6 V. This indicates that the remaining ORR reduction products are likely $\bullet\text{OH}$ species, as suggested by the calculated electron transfer number of around 3. Additionally, as observed in the XPS analysis, a higher carbon xerogel coating correlates with an increased generation of Mn²⁺ species from the reduction of Mn⁴⁺ and Mn³⁺, which

are considered a potent Fenton catalytic sites capable of reducing the generated H₂O₂ to $\bullet\text{OH}$. Based on these results, the C90Mn10 sample has been identified as the most promising catalyst for heterogeneous, bifunctional electro-Fenton applications, making it the material of choice for further study in this context.

3.3. Electro-Fenton reaction for TC degradation

Based on the ORR results, the C90Mn10 sample has been identified as the most promising catalyst for heterogeneous bifunctional electro-Fenton applications (the higher J_K with n of 3), making it the material of choice for further study in this context since it presents the highest ORR kinetic activity and selectivity to H₂O₂ production. In the electro-Fenton experiment, TC was chosen as the target compound, with the potential set to -0.6 eV to achieve both high H₂O₂ selectivity and enhanced activity. Prior to testing, the electrode was saturated with the antibiotic under dark conditions to exclude any adsorptive effects of each sample from influencing the degradation results. Following saturation, the initial TC (C_0) was adjusted to 30 mg L⁻¹, after which the predetermined voltage was applied. This moment marked the initiation of the degradation process. In this way, Fig. 8 illustrates the TC degradation profiles in the electro-Fenton reaction using the C90Mn10 catalyst under different experimental conditions over a total reaction time of 300 min. When nitrogen (N₂) was introduced as the inert gas environment, the TC degradation percentage was relatively low, around 20 %. This outcome is attributed to the limited generation of reactive oxygen species (ROS) in the absence of O₂, highlighting its role in promoting the TC degradation process. As a control test, a traditional Fenton reaction

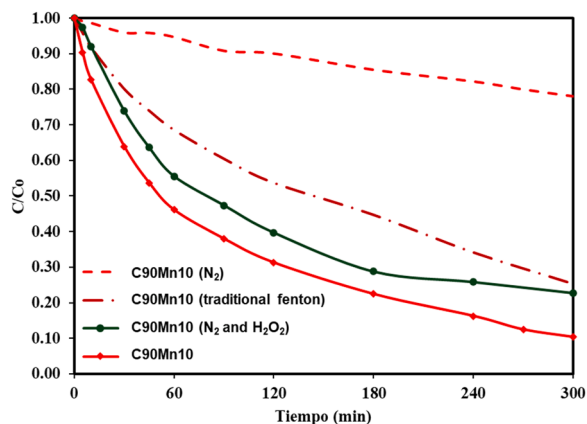


Fig. 8. TC degradation by electro-Fenton with the catalyst C90Mn10 under different experimental conditions.

was conducted in an inert atmosphere with the addition of H_2O_2 , yielding a significantly higher degradation percentage of approximately 74 %. This increase demonstrates the efficiency of the C90Mn10 as Fenton catalyst generating $\bullet OH$ from H_2O_2 without the presence of an applied current. This suggests that the catalytic Mn active sites within the carbon xerogel matrix played a critical role in decomposing H_2O_2 to generate ROS. Nevertheless, this conventional method does not leverage the influence of electric current or the distinctive properties of the C90Mn10 catalyst, particularly its bifunctional catalytic activity. To assess the influence of the current on the degradation efficacy, C90Mn10 catalyst was then evaluated by performing the electro-Fenton reaction under N_2 with the addition of H_2O_2 . Thus, the TC degradation efficiency reached about 78 %, indicating that applied current enhanced the catalyst performance facilitating H_2O_2 decomposition, thereby enhancing $\bullet OH$ production. However, this approach does not utilize the unique properties of the C90Mn10 catalyst, specifically its bifunctional catalytic activity. Finally, the degradation of tetracycline was tested in an O_2 -saturated environment, where the degradation percentage was maximized at 90 %. This high efficiency indicates that O_2 not only acts as a terminal electron acceptor, stabilizing the direct formation of $\bullet OH$ but also facilitates the in-situ generation of H_2O_2 . The combined effect of in-situ H_2O_2 generation and its subsequent reduction to $\bullet OH$ by Mn^{2+} catalytic sites on C90Mn10 optimizes the degradation of tetracycline, confirming the bifunctional nature of this catalyst in the electro-Fenton process. Therefore, two possible pathways are proposed to explain the mechanism of the observed electro-Fenton degradation:

1. Direct in-situ hydroxyl radical generation: The C90Mn10 catalyst, with its carbon xerogel matrix and Mn^{3+} sites, may facilitate a $3e^-$ reduction pathway [56,82]. In this pathway, O_2 is directly reduced to hydroxyl radicals without the intermediate formation of H_2O_2 (Eq. 12). This mechanism would likely involve Mn^{3+} centers and carbon xerogel, both of which act as electron mediators and catalysts in the reaction.



2. Hydrogen peroxide production and subsequent reduction: In this alternative pathway, O_2 is first reduced to H_2O_2 by $2e^-$ route (Eq. 13), followed by the Fenton-like reduction of H_2O_2 to $\bullet OH$, catalyzed by Mn^{2+} active sites on C90Mn10 (Eq. 14) [56]. This sequential process relies on the interaction between Mn^{2+} and H_2O_2 , where Mn^{2+} is regenerated from Mn^{3+} after each catalytic cycle, thereby maintaining a steady generation of hydroxyl radicals.



Considering these outcomes, the amorphous carbon xerogel layer in the C90Mn10 bifunctional electro-Fenton catalyst served multiple purposes that enhanced its catalytic performance. It provided a conductive matrix that facilitates efficient electron transfer, which was essential for maintaining the redox cycles of the Mn^{2+} and Mn^{3+} ions. This conductive layer also promoted the adsorption of TC molecules, allowing for closer interaction with catalytic sites. Furthermore, the carbon coating ensured a controlled and uniform dispersion of MnO_x phases within the matrix, thereby optimizing the availability of active catalytic sites and enhancing the overall catalytic efficacy of the material.

The ICP-OES analysis was conducted to quantify the Mn content in solution, in order to assess potential leaching during the electro-Fenton reaction. Therefore, TC solution at initial time of the experiment an after 300 min of electro-Fenton treatment were taken to carry out the lixiviation study. The Mn concentration remained essentially unchanged, with initial and final values recorded at 1.277 and 1.279 ppm, respectively. This negligible difference confirms the absence of Mn leaching during the reaction, indicating that the structural integrity of the catalyst was preserved throughout the electro-Fenton process. Then, the carbon xerogel coating provides stability to the manganese oxide core, effectively protecting it from potential structural degradation during the catalytic reaction.

Figure S2a presents the cycling experiments for the TC degradation via the electro-Fenton reaction using the C90Mn10 catalyst. The results demonstrate that the catalyst maintains high performance and stability over the first two cycles, achieving degradation rates of approximately 90 % and 86 %, respectively, after 300 min of reaction. This consistent efficiency suggests that the C90Mn10 catalyst possesses a robust structure and catalytic activity that are well-suited for repeated electro-Fenton reactions. In the third cycle, however, the degradation percentage declines to 51 %, likely due to gradual surface passivation or partial loss of active sites after prolonged use. Nonetheless, the strong performance in the initial cycles underscores the catalyst's suitability for short-term applications or batch processes, with potential for further optimization to enhance long-term stability. This performance highlights the promise of C90Mn10 as an effective catalyst for advanced oxidation processes, paving the way for further improvements in catalyst durability.

The toxicity of TC solutions, both prior to and following the electro-Fenton reaction catalyzed by C90Mn10, was evaluated using bioluminescent *Vibrio fischeri* bacteria, as shown in Figure S2b. This analysis provides insight into the potential ecological impact of treated water. Toxicity was measured by the inhibition degree of bacterial bioluminescence, with higher inhibition percentages indicating greater toxicity. The luminescence of the bacteria decreases in response to contaminants, allowing quantification of toxicity based on percentage of luminescence decay. For the initial concentration of TC solution before any electrochemical treatment, bacterial luminescence decreased significantly to 52.5 % after 15 min and further to 42.1 % after 30 min of bacteria incubation, respectively, suggesting high initial toxicity. However, following 300 min of the bifunctional electro-Fenton reaction, the final TC solution showed a notable reduction in toxicity. The bacteria bioluminescence values after 15 and 30 min of incubation were reduced to 76.1 % and 75.1 %, respectively, indicating that the electro-Fenton process effectively decreases the toxicity of the TC solution. The results suggest that while complete mineralization of TC may not be achieved, the degradation products formed exhibit lower toxicity levels, making the treated solution less harmful to aquatic organisms.

The comparative analysis of bifunctional electro-Fenton catalysts presented in Table S2 underscores the exceptional performance of the catalyst developed in this work. Unlike many alternatives that require acidic conditions, our catalyst operated effectively at neutral pH, a key advantage for real-world applications due to its simplicity and environmental compatibility. This distinguishes it as a highly practical

solution for pollutant degradation processes.

Focusing on tetracycline degradation, our catalyst demonstrated remarkable efficiency compared to other reported bifunctional electro-Fenton catalysts. For example, CFF/CNT, a composite of Cu-doped Fe@Fe₂O₃ combined with carbon nanotubes, achieved 98.1 % degradation in 120 min but required a highly acidic environment (pH 3) [83]. Similarly, CCFO, a Cu/CuFe₂O₄ integrated graphite felt, reached 96.3 % efficiency under the same acidic conditions and timeframe [84]. While FeCX-0.8, an Fe-doped carbon xerogel, attained 95.1 % efficiency at near-neutral pH, its reaction time was significantly longer, requiring 420 min [53]. Other catalysts such as CX-6.2, eco-graphene-doped microsphere carbon xerogels [52], and N-CNS-5, nitrogen and eco-graphene co-doped carbon xerogel spheres [55], exhibited lower efficiencies of 83 % and 61.6 %, respectively, despite requiring extended reaction times of 500 and 240 min under near-neutral pH.

In contrast, our bifunctional catalyst C90Mn10 based on carbon-coated manganese microspheres achieved an impressive 90 % tetracycline degradation in just 300 min at neutral pH. This result not only highlights its superior combination of high efficiency and reduced operational time but also underscores its environmental sustainability by eliminating the need for acidic conditions. These attributes position our catalyst as a cutting-edge solution for electro-Fenton processes, offering a practical and effective approach for the degradation of persistent pollutants like tetracycline. Its performance sets a benchmark in the field, demonstrating the potential for more sustainable and efficient wastewater treatment technologies.

4. Conclusions

In conclusion, carbon-coated manganese microspheres were successfully synthesized through a straightforward multi-step process, initially forming Mn spheres via a sonochemical method, followed by coating with carbon xerogel through a resorcinol/formaldehyde sol-gel polymerization in inverse emulsion. The textural, morphological, structural, and surface chemistry properties of the resulting catalysts varied depending on the Mn and carbon xerogel ratios used. Notably, increasing the carbon xerogel content led to enhanced surface area, mesopore volume, and Mn²⁺ content which is identified as a key Fenton catalytic site in the electro-Fenton process. All samples demonstrated ORR activity; however, the C90Mn10 sample exhibited the highest performance in terms of capacitance and kinetic current density, making it the optimal choice for further electro-Fenton testing. The C90Mn10 catalyst demonstrated robust bifunctional activity in the electro-Fenton degradation of TC, achieving a 90 % degradation rate after 300 min of treatment. The catalyst operates through both direct and indirect 3-electron and 2-electron pathways for hydroxyl radical production, respectively, with the carbon xerogel matrix and Mn-based active sites (Mn²⁺ and Mn³⁺) playing complementary roles in ROS generation. This bifunctional mechanism underscores the effectiveness of C90Mn10 as a catalyst in electro-Fenton applications, particularly in systems that demand high efficiency and adaptability for heterogeneous phase reactions. The catalyst showed stable performance over multiple cycles, with only a slight decrease in activity observed after the second cycle, indicating good structural integrity and leaching resistance due to the protective carbon xerogel coating. These findings highlight the potential of C90Mn10 as a promising candidate for environmental remediation technologies, meriting further investigation to maximize its stability and application scope.

CRedit authorship contribution statement

Amaro-Gahete Juan: Writing – original draft, Supervision, Investigation. **Pérez-Cadenas María:** Supervision, Investigation. **Fajardo-Puerto Edgar:** Writing – original draft, Investigation, Data curation. **Elmouwahidi Abdelhakim:** Supervision, Investigation, Conceptualization. **Carrasco-Marín Francisco:** Writing – review & editing,

Validation, Project administration, Funding acquisition, Conceptualization. **Bailón-García Esther:** Writing – review & editing, Validation, Project administration, Funding acquisition, Conceptualization. **Pérez-Cadenas Agustín F.:** Writing – review & editing, Validation, Project administration, Funding acquisition, Conceptualization.

Declaration of Competing Interest

The authors declare that they have no known competing financial interests or personal relationships that could have appeared to influence the work reported in this paper.

Acknowledgements

This research was funded by the Consejería de Universidad, Investigación e Innovación and the ERDF Andalusia Program 2021–2027 under Grant C-EXP-247-UGR23, as well as by MICIU/AEI/10.13039/501100011033, the “European Union NextGenerationEU/PRTR” program, and “ERDF A way of making Europe” under Projects PID2021-127803OB-I00 and CNS2023-144680. A. E. acknowledges the support of the grant María Zambrano (RD 289/2021), funded by the European Union - Next Generation EU programme. J. A-G. would like to thank the “Juan de la Cierva” fellowship with reference JDC2022-048903-I, funded by MCIN/AEI/10.13039/501100011033 and the European Union “NextGenerationEU”/PRTR”. E.B.-G. acknowledges MICINN for her postdoctoral fellowship (RYC2020-029301-I).

Appendix A. Supporting information

Supplementary data associated with this article can be found in the online version at doi:10.1016/j.jece.2025.115725.

Data Availability

No data was used for the research described in the article.

References

- [1] A.H. Khan, H.A. Aziz, N.A. Khan, M.A. Hasan, S. Ahmed, I.H. Farooqi, A. Dhingra, V. Vambol, F. Changani, M. Yousefi, S. Islam, N. Mozaffari, M.S. Mahtab, Impact, disease outbreak and the eco-hazards associated with pharmaceutical residues: a critical review, *Int. J. Environ. Sci. Technol.* 19 (2022) 677–688, <https://doi.org/10.1007/s13762-021-03158-9>.
- [2] B.L. Phoon, C.C. Ong, M.S. Mohamed Saheed, P.-L. Show, J.-S. Chang, T.C. Ling, S. S. Lam, J.C. Juan, Conventional and emerging technologies for removal of antibiotics from wastewater, *J. Hazard. Mater.* 400 (2020) 122961, <https://doi.org/10.1016/j.jhazmat.2020.122961>.
- [3] M.S. de Ilurdoz, J.J. Sadhwani, J.V. Reboso, Antibiotic removal processes from water & wastewater for the protection of the aquatic environment - a review, *J. Water Process Eng.* 45 (2022) 102474, <https://doi.org/10.1016/j.jwpe.2021.102474>.
- [4] R. Gothwal, T. Shashidhar, Antibiotic pollution in the environment: a review, *CLEAN – Soil Air Water* 43 (2015) 479–489, <https://doi.org/10.1002/clean.201300989>.
- [5] M. Pazda, J. Kumirska, P. Stepnowski, E. Mulkiewicz, Antibiotic resistance genes identified in wastewater treatment plant systems – a review, *Sci. Total Environ.* 697 (2019) 134023, <https://doi.org/10.1016/j.scitotenv.2019.134023>.
- [6] Z. Lu, G. Liu, H. Xie, Y. Zhai, X. Li, Advances and solutions in biological treatment for antibiotic wastewater with resistance genes: a review, *J. Environ. Manag.* 368 (2024) 122115, <https://doi.org/10.1016/j.jenvman.2024.122115>.
- [7] R. Daghri, P. Drogui, Tetracycline antibiotics in the environment: a review, *Environ. Chem. Lett.* 11 (2013) 209–227, <https://doi.org/10.1007/s10311-013-0404-8>.
- [8] A.A. Borghi, M.S.A. Palma, Tetracycline: production, waste treatment and environmental impact assessment, *Braz. J. Pharm. Sci.* 50 (2014) 25–40, <https://doi.org/10.1590/S1984-82502011000100003>.
- [9] Y. Dai, M. Liu, J. Li, S. Yang, Y. Sun, Q. Sun, W. Wang, L. Lu, K. Zhang, J. Xu, W. Zheng, Z. Hu, Y. Yang, Y. Gao, Z. Liu, A review on pollution situation and treatment methods of tetracycline in groundwater, *Sep. Sci. Technol.* 55 (2020) 1005–1021, <https://doi.org/10.1080/01496395.2019.1577445>.
- [10] L. Xu, H. Zhang, P. Xiong, Q. Zhu, C. Liao, G. Jiang, Occurrence, fate, and risk assessment of typical tetracycline antibiotics in the aquatic environment: a review, *Sci. Total Environ.* 753 (2021) 141975, <https://doi.org/10.1016/j.scitotenv.2020.141975>.

- [11] S.M. Ebrahimi, R. Dehghanzadeh Reyhani, M. Asghari-JafarAbadi, Z. Fathifar, Diversity of antibiotics in hospital and municipal wastewaters and receiving water bodies and removal efficiency by treatment processes: a systematic review protocol, *Environ. Evid.* 9 (2020) 19, <https://doi.org/10.1186/s13750-020-00201-z>.
- [12] F. Ahmad, D. Zhu, J. Sun, Environmental fate of tetracycline antibiotics: degradation pathway mechanisms, challenges, and perspectives, *Environ. Sci. Eur.* 33 (2021) 64, <https://doi.org/10.1186/s12302-021-00505-y>.
- [13] J. Rivera-Utrilla, R. Ocampo-Perez, M. Sanchez-Polo, J.J. Lopez-Penalver, C. V. Gomez-Pacheco, Removal of tetracyclines from water by adsorption/bioadsorption and advanced oxidation processes. A short review, *Curr. Org. Chem.* 22 (2018) 1005–1021, <https://doi.org/10.2174/1385272822666180322124243>.
- [14] E.M. Cuerva-Correa, M.F. Alexandre-Franco, C. Fernández-González, Advanced oxidation processes for the removal of antibiotics from water. An overview, *Water* 12 (2019) 102, <https://doi.org/10.3390/w12010102>.
- [15] G. Gopal, S.A. Alex, N. Chandrasekaran, A. Mukherjee, A review on tetracycline removal from aqueous systems by advanced treatment techniques, *RSC Adv.* 10 (2020) 27081–27095, <https://doi.org/10.1039/D0RA04264A>.
- [16] J. Wang, R. Zhuang, Degradation of antibiotics by advanced oxidation processes: an overview, *Sci. Total Environ.* 701 (2020) 135023, <https://doi.org/10.1016/j.scitotenv.2019.135023>.
- [17] L. Blaney, Ozone treatment of antibiotics in water. *Water Reclam. Sustain.*, Elsevier, 2014, pp. 265–316, <https://doi.org/10.1016/B978-0-12-411645-0.00012-2>.
- [18] J.O. Adeyemi, T. Ajiboye, D.C. Onwudiwe, Mineralization of antibiotics in wastewater via photocatalysis, *Water Air Soil Pollut.* 232 (2021) 219, <https://doi.org/10.1007/s11270-021-05167-3>.
- [19] Y. Jiang, J. Ran, K. Mao, X. Yang, L. Zhong, C. Yang, X. Feng, H. Zhang, Recent progress in Fenton/Fenton-like reactions for the removal of antibiotics in aqueous environments, *Ecotoxicol. Environ. Saf.* 236 (2022) 113464, <https://doi.org/10.1016/j.ecoenv.2022.113464>.
- [20] Z. Honarmandrad, X. Sun, Z. Wang, M. Naushad, G. Boczkaj, Activated persulfate and peroxymonosulfate based advanced oxidation processes (AOPs) for antibiotics degradation – a review, *Water Resour. Ind.* 29 (2023) 100194, <https://doi.org/10.1016/j.wri.2022.100194>.
- [21] M. Zhang, H. Dong, L. Zhao, D. Wang, D. Meng, A review on Fenton process for organic wastewater treatment based on optimization perspective, *Sci. Total Environ.* 670 (2019) 110–121, <https://doi.org/10.1016/j.scitotenv.2019.03.180>.
- [22] U. Razaq, T.-B. Nguyen, M.-U. Saleem, V.-R. Le, C.-W. Chen, X.-T. Bui, C.-D. Dong, Recent progress in electro-Fenton technology for the remediation of pharmaceutical compounds in aqueous environments, *Sci. Total Environ.* 946 (2024) 174253, <https://doi.org/10.1016/j.scitotenv.2024.174253>.
- [23] P.V. Nidheesh, H. Olvera-Vargas, N. Oturan, M.A. Oturan, Heterogeneous electro-fenton process: principles and applications. *Handb. Environ. Chem.*, Springer Verlag, 2017, pp. 85–110, <https://doi.org/10.1007/978-2017-72>.
- [24] S.O. Ganiyu, M. Zhou, C.A. Martínez-Huitle, Heterogeneous electro-Fenton and photoelectro-Fenton processes: a critical review of fundamental principles and application for water/wastewater treatment, *Appl. Catal. B.* 235 (2018) 103–129, <https://doi.org/10.1016/j.apcatb.2018.04.044>.
- [25] K.M. Nair, V. Kumaravel, S.C. Pillai, Carbonaceous cathode materials for electro-Fenton technology: Mechanism, kinetics, recent advances, opportunities and challenges, *Chemosphere* 269 (2021) 129325, <https://doi.org/10.1016/j.chemosphere.2020.129325>.
- [26] S. Karthikeyan, M.P. Pachamuthu, M.A. Isaacs, S. Kumar, A.F. Lee, G. Sekaran, Cu and Fe oxides dispersed on SBA-15: a fenton type bimetallic catalyst for N,N-diethyl- p-phenyl diamine degradation, *Appl. Catal. B* 199 (2016) 323–330, <https://doi.org/10.1016/j.apcatb.2016.06.040>.
- [27] H. Bel Hadjiltaief, P. Da Costa, P. Beaunier, M.E. Gálvez, M. Ben Zina, Fe-clay-plate as a heterogeneous catalyst in photo-Fenton oxidation of phenol as probe molecule for water treatment, *Appl. Clay Sci.* 91–92 (2014) 46–54, <https://doi.org/10.1016/j.clay.2014.01.020>.
- [28] M.A. Fontecha-Cámara, M.A. Álvarez-Merino, F. Carrasco-Marín, M.V. López-Ramón, C. Moreno-Castilla, Heterogeneous and homogeneous Fenton processes using activated carbon for the removal of the herbicide amitrole from water, *Appl. Catal. B* 101 (2011) 425–430, <https://doi.org/10.1016/j.apcatb.2010.10.012>.
- [29] Z. Pan, X. Qian, Porous carbons for use in electro-Fenton and Fenton-like reactions, *N. Carbon Mater.* 37 (2022) 180–195, [https://doi.org/10.1016/S1872-5805\(22\)60578-X](https://doi.org/10.1016/S1872-5805(22)60578-X).
- [30] S. Guo, G. Zhang, Y. Guo, J.C. Yu, Graphene oxide–Fe₂O₃ hybrid material as highly efficient heterogeneous catalyst for degradation of organic contaminants, *Carbon* N. Y. 60 (2013) 437–444, <https://doi.org/10.1016/j.carbon.2013.04.058>.
- [31] G. Divyapriya, P.V. Nidheesh, Importance of graphene in the electro-fenton process, *ACS Omega* 5 (2020) 4725–4732, <https://doi.org/10.1021/acsomega.9b04201>.
- [32] B. Garza-Campos, D. Morales-Acosta, A. Hernández-Ramírez, J.L. Guzmán-Mar, L. Hinojosa-Reyes, J. Manríquez, E.J. Ruiz-Ruiz, Air diffusion electrodes based on synthesized mesoporous carbon for application in amoxicillin degradation by electro-Fenton and solar photo electro-Fenton, *Electrochim. Acta* 269 (2018) 232–240, <https://doi.org/10.1016/j.electacta.2018.02.139>.
- [33] S. Chen, L. Tang, H. Feng, Y. Zhou, G. Zeng, Y. Lu, J. Yu, X. Ren, B. Peng, X. Liu, Carbon felt cathodes for electro-Fenton process to remove tetracycline via synergistic adsorption and degradation, *Sci. Total Environ.* 670 (2019) 921–931, <https://doi.org/10.1016/j.scitotenv.2019.03.086>.
- [34] L. Gu, N. Zhu, H. Guo, S. Huang, Z. Lou, H. Yuan, Adsorption and Fenton-like degradation of naphthalene dye intermediate on sewage sludge derived porous carbon, *J. Hazard. Mater.* 246–247 (2013) 145–153, <https://doi.org/10.1016/j.jhazmat.2012.12.012>.
- [35] H. Zhao, Y. Wang, Y. Wang, T. Cao, G. Zhao, Electro-Fenton oxidation of pesticides with a novel Fe₃O₄@Fe₂O₃/activated carbon aerogel cathode: High activity, wide pH range and catalytic mechanism, *Appl. Catal. B.* 125 (2012) 120–127, <https://doi.org/10.1016/j.apcatb.2012.05.044>.
- [36] N. Fernández-Sáez, D.E. Villela-Martínez, F. Carrasco-Marín, A.F. Pérez-Cadenas, L. M. Pastrana-Martínez, Heteroatom-doped graphene aerogels and carbon-magnetite catalysts for the heterogeneous electro-Fenton degradation of acetaminophen in aqueous solution, *J. Catal.* 378 (2019) 68–79, <https://doi.org/10.1016/j.jcat.2019.08.020>.
- [37] Y. Okamoto, First-principles molecular dynamics simulation of O₂ reduction on nitrogen-doped carbon, *Appl. Surf. Sci.* 256 (2009) 335–341, <https://doi.org/10.1016/j.apsusc.2009.08.027>.
- [38] A. Zahoor, M. Christy, Y.J. Hwang, Y.R. Lim, P. Kim, K.S. Nahm, Improved electrocatalytic activity of carbon materials by nitrogen doping, *Appl. Catal. B.* 147 (2014) 633–641, <https://doi.org/10.1016/j.apcatb.2013.09.043>.
- [39] X. Wang, G. Sun, P. Routh, D.-H. Kim, W. Huang, P. Chen, Heteroatom-doped graphene materials: syntheses, properties and applications, *Chem. Soc. Rev.* 43 (2014) 7067–7098, <https://doi.org/10.1039/C4CS00141A>.
- [40] L.T. Soo, K.S. Loh, A.B. Mohamad, W.R.W. Daud, W.Y. Wong, An overview of the electrochemical performance of modified graphene used as an electrocatalyst and as a catalyst support in fuel cells, *Appl. Catal. A.* 497 (2015) 198–210, <https://doi.org/10.1016/j.apcata.2015.03.008>.
- [41] P. Su, M. Zhou, X. Lu, W. Yang, G. Ren, J. Cai, Electrochemical catalytic mechanism of N-doped graphene for enhanced H₂O₂ yield and in-situ degradation of organic pollutant, *Appl. Catal. B.* 245 (2019) 583–595, <https://doi.org/10.1016/j.apcatb.2018.12.075>.
- [42] M. Qin, S. Fan, L. Wang, G. Gan, X. Wang, J. Cheng, Z. Hao, X. Li, Oxygen and nitrogen co-doped ordered mesoporous carbon materials enhanced the electrochemical selectivity of O₂ reduction to H₂O₂, *J. Colloid Interface Sci.* 562 (2020) 540–549, <https://doi.org/10.1016/j.jcis.2019.11.080>.
- [43] Y. Zhu, F. Deng, S. Qiu, F. Ma, Y. Zheng, R. Lian, Enhanced electro-Fenton degradation of sulfonamides using the N, S co-doped cathode: mechanism for H₂O₂ formation and pollutants decay, *J. Hazard. Mater.* 403 (2021) 123950, <https://doi.org/10.1016/j.jhazmat.2020.123950>.
- [44] S. Song, M. Wu, Y. Liu, Q. Zhu, P. Tsiakaras, Y. Wang, Efficient and stable carbon-coated nickel foam cathodes for the electro-fenton process, *Electrochim. Acta* 176 (2015) 811–818, <https://doi.org/10.1016/j.electacta.2015.07.029>.
- [45] C. Zhang, M. Zhou, X. Yu, L. Ma, F. Yu, Modified iron-carbon as heterogeneous electro-Fenton catalyst for organic pollutant degradation in near neutral pH condition: characterization, degradation activity and stability, *Electrochim. Acta* 160 (2015) 254–262, <https://doi.org/10.1016/j.electacta.2015.01.092>.
- [46] Z. Han, Z. Li, Y. Li, D. Shang, L. Xie, Y. Lv, S. Zhan, W. Hu, Enhanced electron transfer and hydrogen peroxide activation capacity with N, P-codoped carbon encapsulated CeO₂ in heterogeneous electro-Fenton process, *Chemosphere* 287 (2022) 132154, <https://doi.org/10.1016/j.chemosphere.2021.132154>.
- [47] J. Guo, G. Song, X. Zhang, M. Zhou, Transition metal catalysts in the heterogeneous electro-Fenton process for organic wastewater treatment: a review, *Environ. Sci. Water Res. Technol.* 9 (2023) 2429–2445, <https://doi.org/10.1039/D3EW00302G>.
- [48] X. Luo, R. Zhu, L. Zhao, X. Gong, Dual-functional electrocatalyst of defective cobalt-nitrogen-doped porous carbon for enhanced in-situ hydrogen peroxide generation and electro-Fenton tetracycline degradation, *Sep. Purif. Technol.* 346 (2024) 127451, <https://doi.org/10.1016/j.seppur.2024.127451>.
- [49] Y. Liu, C. Kong, L. Liu, X. Jiang, C. Liu, F. Liu, J. Sun, Y. Wang, Progress in copper-based supported heterogeneous electro-Fenton catalysts, *Chem. Eng. J.* 486 (2024) 150217, <https://doi.org/10.1016/j.cej.2024.150217>.
- [50] Y. Yao, Y. Pan, Y. Yu, Z. Yu, L. Lai, F. Liu, L. Wei, Y. Chen, Bifunctional catalysts for heterogeneous electro-Fenton processes: a review, *Environ. Chem. Lett.* 20 (2022) 3837–3859, <https://doi.org/10.1007/s10311-022-01453-6>.
- [51] E. Fajardo-Puerto, A. Elmouwahidi, E. Bailón-García, A.F. Pérez-Cadenas, F. Carrasco-Marín, From Fenton and ORR 2e⁻-type catalysts to bifunctional electrodes for environmental remediation using the electro-fenton process, *Catalysts* 13 (2023) 674, <https://doi.org/10.3390/catal13040674>.
- [52] L.D. Ramírez-Valencia, E. Bailón-García, A.I. Moral-Rodríguez, F. Carrasco-Marín, A.F. Pérez-Cadenas, Carbon gels–green graphene composites as metal-free bifunctional electro-fenton catalysts, *Gels* 9 (2023) 665, <https://doi.org/10.3390/gels9080665>.
- [53] A. Barranco-López, A.I. Moral-Rodríguez, E. Fajardo-Puerto, A. Elmouwahidi, E. Bailón-García, Highly graphitic Fe-doped carbon xerogels as dual-functional electro-Fenton catalysts for the degradation of tetracycline in wastewater, *Environ. Res.* 228 (2023) 115757, <https://doi.org/10.1016/j.envres.2023.115757>.
- [54] L.C. Valencia-Valero, E. Fajardo-Puerto, A. Elmouwahidi, E. Bailón-García, F. Carrasco-Marín, A.F. Pérez-Cadenas, Facile synthesis of carbon-based inks to develop metal-free ORR electrocatalysts for electro-fenton removal of Amoxicillin, *Gels* 10 (2024) 53, <https://doi.org/10.3390/gels10010053>.
- [55] E. Fajardo-Puerto, N. López-García, A. Elmouwahidi, E. Bailón-García, F. Carrasco-Marín, L.D. Ramírez-Valencia, A.F. Pérez-Cadenas, Size control of carbon xerogel spheres as key factor governing the H₂O₂ selectivity in metal-free bifunctional electro-fenton catalysts for tetracycline degradation, *Gels* 10 (2024) 306, <https://doi.org/10.3390/gels10050306>.
- [56] E. Fajardo-Puerto, A. Elmouwahidi, E. Bailón-García, M. Pérez-Cadenas, A.F. Pérez-Cadenas, F. Carrasco-Marín, Antibiotic degradation via fenton process assisted by a 3-electron oxygen reduction reaction pathway catalyzed by bio-carbon–manganese composites, *Nanomaterials* 14 (2024) 1112, <https://doi.org/10.3390/nano14131112>.

- [57] A. Elmouwahidi, E. Bailón-García, A.F. Pérez-Cadenas, J. Castelo-Quibén, F. Carrasco-Marín, Carbon-vanadium composites as non-precious catalysts for electro-reduction of oxygen, *Carbon N. Y* 144 (2019) 289–300, <https://doi.org/10.1016/j.carbon.2018.12.038>.
- [58] A. Elmouwahidi, E. Bailón-García, A.F. Pérez-Cadenas, A. Celzard, V. Fierro, F. Carrasco-Marín, Carbon microspheres with tailored texture and surface chemistry as electrode materials for supercapacitors, *ACS Sustain. Chem. Eng.* 9 (2021) 541–551, <https://doi.org/10.1021/acssuschemeng.0c08024>.
- [59] R. Zhou, Y. Zheng, M. Jaroniec, S.-Z. Qiao, Determination of the electron transfer number for the oxygen reduction reaction: from theory to experiment, *ACS Catal.* 6 (2016) 4720–4728, <https://doi.org/10.1021/acscatal.6b01581>.
- [60] K. Jiang, S. Back, A.J. Akey, C. Xia, Y. Hu, W. Liang, D. Schaak, E. Stavitski, J. K. Nørskov, S. Siahrostami, H. Wang, Highly selective oxygen reduction to hydrogen peroxide on transition metal single atom coordination, *Nat. Commun.* 10 (2019) 3997, <https://doi.org/10.1038/s41467-019-11992-2>.
- [61] S. Brocato, C. Lau, P. Atanassov, Mechanistic study of direct electron transfer in bilirubin oxidase, *Electrochim. Acta* 61 (2012) 44–49, <https://doi.org/10.1016/j.electacta.2011.11.074>.
- [62] S. Xu, Y. Kim, D. Higgins, M. Yusuf, T.F. Jaramillo, F.B. Prinz, Building upon the Koutecky-Levich equation for evaluation of next-generation oxygen reduction reaction catalysts, *Electrochim. Acta* 255 (2017) 99–108, <https://doi.org/10.1016/j.electacta.2017.09.145>.
- [63] J. Fan, Q. Ren, S. Mo, Y. Sun, M. Fu, J. Wu, L. Chen, P. Chen, D. Ye, Transient in-situ DRIFTS investigation of catalytic oxidation of toluene over α -, γ - and β -MnO₂, *ChemCatChem* 12 (2020) 1046–1054, <https://doi.org/10.1002/cctc.201901839>.
- [64] A. Elmouwahidi, E. Bailón-García, A.F. Pérez-Cadenas, A. Celzard, V. Fierro, F. Carrasco-Marín, Carbon microspheres with tailored texture and surface chemistry as electrode materials for supercapacitors, *ACS Sustain. Chem. Eng.* 9 (2021) 541–551, <https://doi.org/10.1021/acssuschemeng.0c08024>.
- [65] E. Bailón-García, A. Elmouwahidi, M.A. Álvarez, F. Carrasco-Marín, A.F. Pérez-Cadenas, F.J. Maldonado-Hódar, New carbon xerogel-TiO₂ composites with high performance as visible-light photocatalysts for dye mineralization, *Appl. Catal. B.* 201 (2017) 29–40, <https://doi.org/10.1016/j.apcatb.2016.08.015>.
- [66] H.-W. Liang, W. Wei, Z.-S. Wu, X. Feng, K. Müllen, Mesoporous metal–nitrogen-doped carbon electrocatalysts for highly efficient oxygen reduction reaction, *J. Am. Chem. Soc.* 135 (2013) 16002–16005, <https://doi.org/10.1021/ja407552k>.
- [67] M. Zhang, L. Xu, C. Qi, M. Zhang, Highly effective removal of tetracycline from water by hierarchical porous carbon: batch and column adsorption, *Ind. Eng. Chem. Res.* 58 (2019) 20036–20046, <https://doi.org/10.1021/acs.iecr.9b03547>.
- [68] J. Castelo-Quibén, E. Bailón-García, F.J. Pérez-Fernández, F. Carrasco-Marín, A. F. Pérez-Cadenas, Mesoporous carbon nanospheres with improved conductivity for electro-catalytic reduction of O₂ and CO₂, *Carbon N. Y* 155 (2019) 88–99, <https://doi.org/10.1016/j.carbon.2019.08.007>.
- [69] Z. Zapata-Benabithé, F. Carrasco-Marín, J. de Vicente, C. Moreno-Castilla, Carbon xerogel microspheres and monoliths from resorcinol–formaldehyde mixtures with varying dilution ratios: preparation, surface characteristics, and electrochemical double-layer capacitances, *Langmuir* 29 (2013) 6166–6173, <https://doi.org/10.1021/la4007422>.
- [70] J. Wang, D. Zhang, F. Nie, R. Zhang, X. Fang, Y. Wang, The role of MnO₂ crystal morphological scale and crystal structure in selective catalytic degradation of azo dye, *Environ. Sci. Pollut. Res.* 30 (2022) 15377–15391, <https://doi.org/10.1007/s11356-022-23223-1>.
- [71] Y. Hua, Y. Ahmadi, K. Kim, Thermocatalytic degradation of gaseous formaldehyde using transition metal-based catalysts, *Adv. Sci.* 10 (2023) 2300079, <https://doi.org/10.1002/advs.202300079>.
- [72] G. Huo, X.-W. Wang, Z.-B. Zhang, Z. Song, X.-M. Kang, M.-X. Chen, Q. Wang, X.-Z. Fu, J.-L. Luo, γ -MnO₂ nanorod-assembled hierarchical micro-spheres with oxygen vacancies to enhance electrocatalytic performance toward the oxygen reduction reaction for aluminum-air batteries, *J. Energy Chem.* 51 (2020) 81–89, <https://doi.org/10.1016/j.jechem.2020.03.030>.
- [73] J. Yang, X. Yang, Y.L. Zhong, J.Y. Ying, Porous MnO/Mn₃O₄ nanocomposites for electrochemical energy storage, *Nano Energy* 13 (2015) 702–708, <https://doi.org/10.1016/j.nanoen.2015.03.026>.
- [74] R. Tholkappiyam, A.N. Naveen, K. Vishista, F. Hamed, Investigation on the electrochemical performance of hausmannite Mn₃O₄ nanoparticles by ultrasonic irradiation assisted co-precipitation method for supercapacitor electrodes, *J. Taibah Univ. Sci.* 12 (2018) 669–677, <https://doi.org/10.1080/16583655.2018.1497440>.
- [75] L.V. Stebounova, N.I. Gonzalez-Pech, T.M. Peters, V.H. Grassian, Physicochemical properties of air discharge-generated manganese oxide nanoparticles: comparison to welding fumes, *Environ. Sci. Nano.* 5 (2018) 696–707, <https://doi.org/10.1039/C7EN01046J>.
- [76] Y. Lin, S. Su, Y. Cui, H. Dai, L. Lai, X. Zhu, Regulating manganese valence in MnOx/rGO composite for high-performance supercapacitors, *J. Mater. Sci. Mater. Electron.* 34 (2023) 1308, <https://doi.org/10.1007/s10854-023-10747-6>.
- [77] S. Ncube, M. Moyo, A review of the use of carbon nanostructures and other reducing agents during auto-reduction for Fischer–Tropsch synthesis and other applications, *Catal. Lett.* 154 (2024) 366–386, <https://doi.org/10.1007/s10562-023-04330-1>.
- [78] C.W. Woon, M.A. Islam, B. Ethiraj, H.R. Ong, C.K. Cheng, K.F. Chong, G. Hedge, M. M.R. Khan, Carbon nanotube-modified MnO₂: an efficient electrocatalyst for oxygen reduction reaction, *ChemistrySelect* 2 (2017) 7637–7644, <https://doi.org/10.1002/slct.201700741>.
- [79] M.R. Majidi, F. Shabbazi Farahani, M. Hosseini, I. Ahadzadeh, Low-cost nanowired α -MnO₂/C as an ORR catalyst in air-cathode microbial fuel cell, *Bioelectrochemistry* 125 (2019) 38–45, <https://doi.org/10.1016/j.bioelechem.2018.09.004>.
- [80] G. Ramos-Fernández, M. Canal-Rodríguez, A. Arenillas, J.A. Menéndez, I. Rodríguez-Pastor, I. Martín-Gullón, Determinant influence of the electrical conductivity versus surface area on the performance of graphene oxide-doped carbon xerogel supercapacitors, *Carbon N. Y.* 126 (2018) 456–463, <https://doi.org/10.1016/j.carbon.2017.10.025>.
- [81] J. Amaro-Gahete, J.A. Salatti-Dorado, A. Benítez, D. Esquivel, V. García-Caballero, M. López-Haro, J.J. Delgado, M. Cano, J.J. Giner-Casares, F.J. Romero-Salguero, Surface Diels–Alder adducts on multilayer graphene for the generation of edge-enriched single-atom FeN₄ sites for ORR and OER electrocatalysis, *Sustain. Energy Fuels* 6 (2022) 1603–1615, <https://doi.org/10.1039/D2SE00004K>.
- [82] F. Xie, Y. Gao, J. Zhang, H. Bai, J. Zhang, Z. Li, W. Zhu, A novel bifunctional cathode for the generation and activation of H₂O₂ in electro-Fenton: characteristics and mechanism, *Electrochim. Acta* 430 (2022) 141099, <https://doi.org/10.1016/j.electacta.2022.141099>.
- [83] T. Luo, H. Feng, L. Tang, Y. Lu, W. Tang, S. Chen, J. Yu, Q. Xie, X. Ouyang, Z. Chen, Efficient degradation of tetracycline by heterogeneous electro-Fenton process using Cu-doped Fe@Fe₂O₃: mechanism and degradation pathway, *Chem. Eng. J.* 382 (2020) 122970, <https://doi.org/10.1016/j.cej.2019.122970>.
- [84] L. Cui, Z. Li, Q. Li, M. Chen, W. Jing, X. Gu, Cu/CuFe₂O₄ integrated graphite felt as a stable bifunctional cathode for high-performance heterogeneous electro-Fenton oxidation, *Chem. Eng. J.* 420 (2021) 127666, <https://doi.org/10.1016/j.cej.2020.127666>.